1 Supporting Information for

2

3 **Dependence of Thermoelectric Effects in Molecular Junctions on the Topography of the**

4 **Bottom-Electrodes**

5

6 Wuxian Peng, Zhou Cao, Ningyue Chen, Yu Xie and Yuan Li[*]

7

8 Department of Chemistry, Tsinghua University, Beijing 10084, China

9

10 *Corresponding author, Email: yuanli_thu@tsinghua.edu.cn

11

12

13 **S1. Synthesis**.

14 **Thiophenol (HS(Ph)$_1$).** We synthesized thiophenol according to a procedure reported in the

15 literature.[1] Bromobenzene (2.00 mL, 20.00 mmol), ethane-1, 2-dithiol (2.01 mL 24.00 mmol),

16 KOH (5.60 g, 100.00 mmol) and CuSO$_4$·5H$_2$O (0.16 g, 5 mol%), were heated at 120 °C in DMF

17 (50.00 mL) under N$_2$ for 24 hours. The mixture was extracted three times with CH$_2$Cl$_2$ (3 × 100

18 mL), washed with brine (3 × 100 mL) after cooling down to room temperature. The combined

19 organic phases were then dried over Na$_2$SO$_4$, filtered and concentrated under reduced pressure.

20 The product thiophenol (0.24 g, yield 11.0%) was then purified by column chromatography

21 (silica gel, CH$_2$Cl$_2$/petroleum ether = 1/2 v/v). 1H NMR (400 MHz, DMSO-d6) δ 7.56 – 7.49

22 (m, 2H), 7.39 (t, J = 7.7 Hz, 2H), 7.34 – 7.25 (m, 1H). HRMS (ESI$^+$): m/z calc for C$_6$H$_7$S

23 [M+H]$^+$ 111.0268, found 111.0257.

24
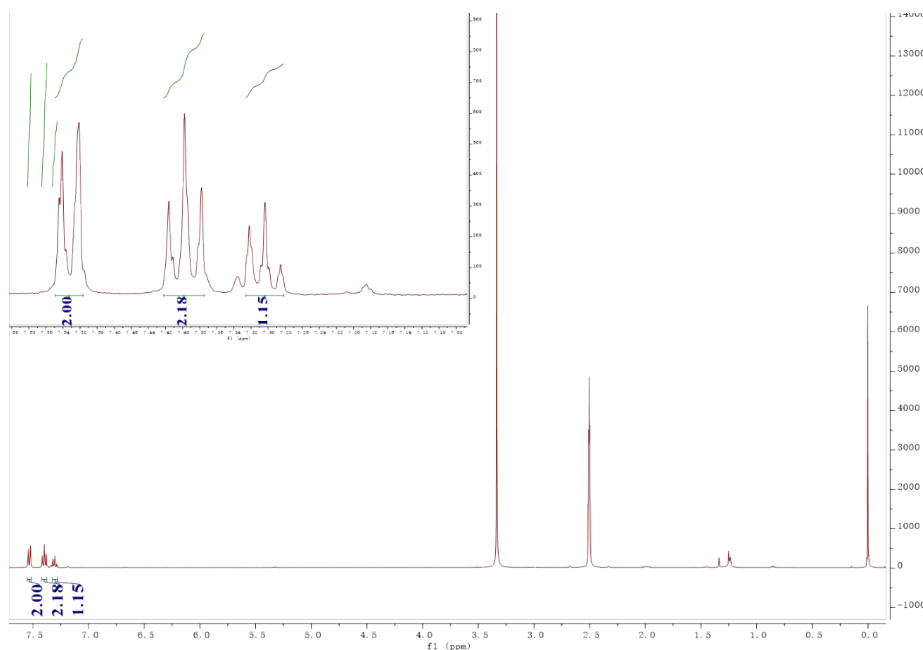
26 **Fig. S1.** ^{1}H NMR spectrum for HS(Ph)$_1$ in DMSO.

27
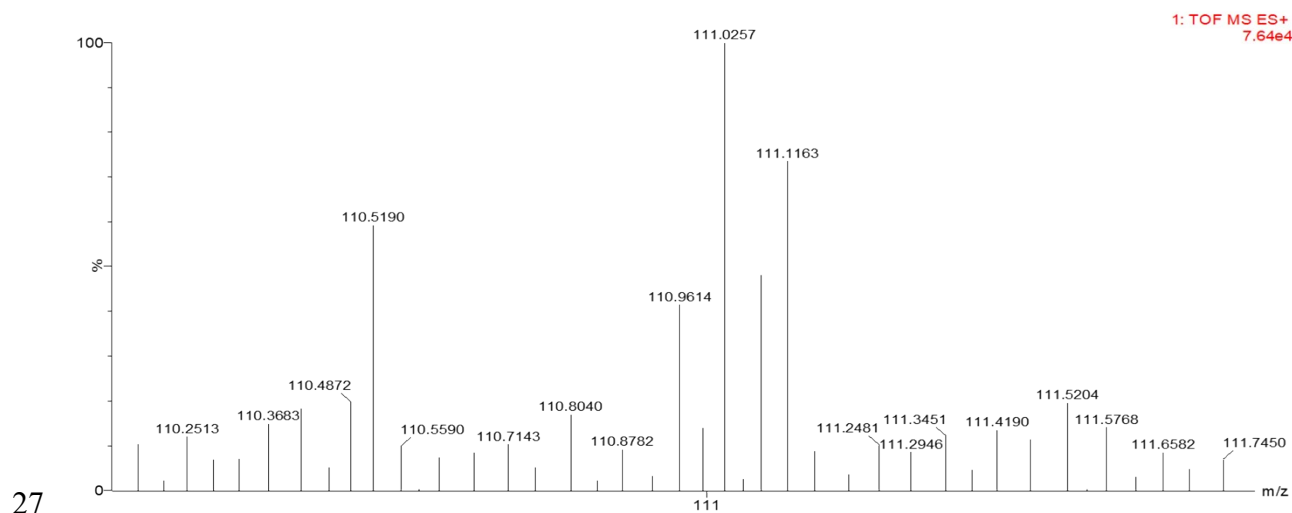
Fig. S2. The HRMS spectrum of $HS(Ph)_1$.

28

29

30 **4-Terphenylthiol ($HS(Ph)_3$).** We synthesized 4-Terphenylthiol by the same procedure of

31 $HS(Ph)_1$.[1] 4-bromo-p-terphenyl (3.09, 10.00 mmol), ethane-1,2-dithiol (1.00 mL 12.00 mmol),

32 KOH (2.80 g, 50.00 mmol) and $CuSO_4 \cdot 5H_2O$ (0.08 g, 5 mol%), were heated at 120 °C in DMF

33 (30.00 mL) under N_2 for 24 hours. The mixture was extracted three times with CH_2Cl_2 (3 × 100

34 mL), washed with brine (3 × 100 mL) after cooling down to room temperature. The combined

35 organic phases were then dried over Na_2SO_4, filtered and concentrated under reduced pressure.

36 The product thiophenol (0.24 g, yield 9.0%) was then purified by column chromatography

37 (silica gel, CH_2Cl_2/petroleum ether = 1/2 v/v). ^{1}H NMR (400 MHz, Chloroform-*d*) δ 7.70 – 7.61

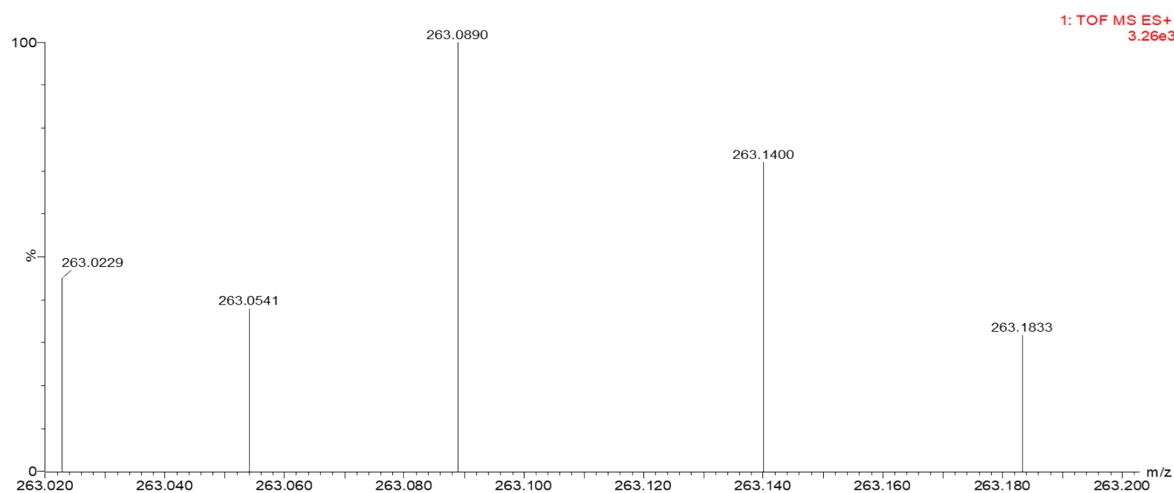38 (m, 6H), 7.58 (d, *J* = 8.5 Hz, 2H), 7.46 (t, *J* = 7.6 Hz, 2H), 7.35 (d, *J* = 8.5 Hz, 3H). HRMS

39 (ESI$^+$): m/z calc for $C_{18}H_{15}S$ [M+H]$^+$ 263.089, found 263.089.
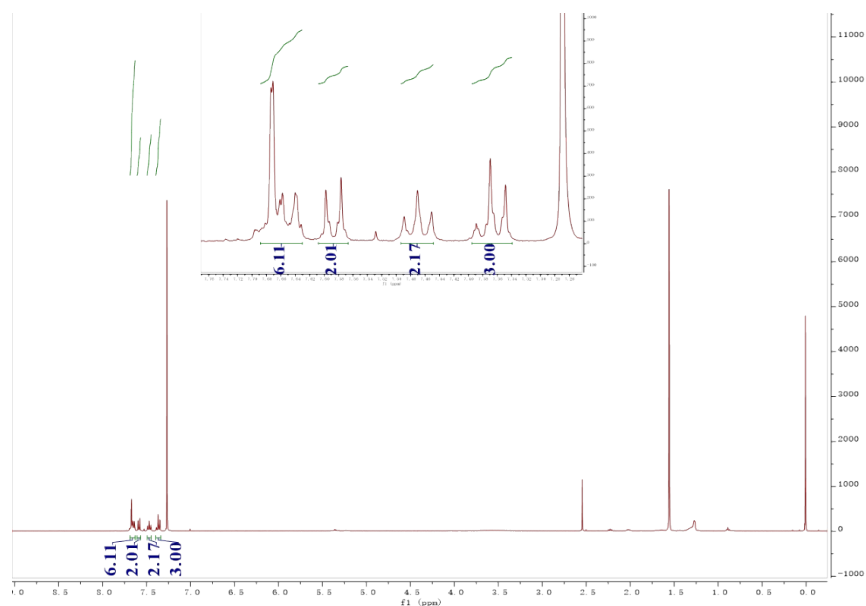
40

41 **Fig. S3.** ^{1}H NMR spectrum for HS(Ph)$_3$ in CDCl$_3$.

42

43

44 **Fig. S4.** The HRMS spectrum of HS(Ph)$_3$.

45

46 **S2. Sample preparations**.

47 **Template-stripped Au surfaces (Au^{TS}).** Au^{TS} substrates were prepared following procedures

48 reported previously.[2] Briefly, we deposited a 200 nm thick Au (Au with a purity of 99.999%

49 from Dimu Materials, Inc (China)) film on clean Si (100) wafers with a native SiO$_2$ surface

50 layer by thermal deposition (KYKY-400, Zhongke Ke Yi, China) with the base pressure being

51 2×10^{-5} Pa and the evaporation rate was about 0.2 Å s^{-1} for Au at the first 50 nm and then

52 increased to ~1 Å s^{-1} for the rest 150 nm. The glass slides (1.5 × 1.5 cm^2) were ultrasonically

53 cleaned with acetone and then ethanol for 20 minutes, and the slides were blown to dryness in

54 a stream of N$_2$ gas. After we cleaned the glass slides by a plasma of air for 5 mins at a pressure

55 of 100 Pa, the glass slides were glued on the Au surfaces by photo-curable optical adhesive

56 (Norland, No. 61). A 100 Watt UV lamp was used to cure the optical adhesive for 1 hour at a

57 distance of 60 cm from the light source. The Au surface that had been in contact with the Si/SiO$_2$

58 wafer was lift-off by a razor blade.

59 **Direct deposition of Au (Au^{DE}).** As described before,[3] the thermal evaporator was applied to

60 deposit Au on the Si wafers under high vacuum (2 × 10^{-5} mbar) and the deposition rate and film

61 thickness were two significant parameters to determine the surface roughness, and the receipt

62 we used for i) Au^{DE1} (rms = 1.3 nm, a 5 nm layer of Cr at rate of 0.1 Å s^{-1} followed by 200 nm

63 of Au at a rate of 1 Å s^{-1}), ii) Au^{DE2} (rms = 2.2 nm, a 20 nm layer of Cr at rate of 1 Å s^{-1} followed

64 by 200   nm of Au at a rate of 5 Å s^{-1}) and iii) Au^{DE3} (rms = 3.2 nm, a 40 nm layer of Cr at rate

65 of 1 Å s^{-1} followed by 400 nm of Au at a rate of 5 Å s^{-1}). To eliminate surface contamination

66 from the ambient, the Au^{DE} surfaces removing from the vacuum chamber were immediately

67 used to form SAMs.

68 **SAMs preparation.** All thiol terminated molecules except HS(Ph)$_1$ and HS(Ph)$_3$ were

69 purchased from Sigma Aldrich with their highest purity (at least >98%) that we can found. To

70 form SAMs, Au substrates were immersed in degassed 3 mM ethanolic solutions of HSC$_m$ (m

71 = 4, 6, 8) and HS(Ph)$_n$ (n = 1, 2, 3) over a period of time of 3 h under an inert nitrogen

72 environment. The SAMs were rinsed with ethanol (AR grade) to remove the physisorbed

73 molecules, dried in a stream of dry nitrogen gently and used for experiments within minutes to

74 avoid degradation of the S-Au bond and surface contaminations.

75

76

77 **S3. Sample Characterizations**.

78 **Atomic Force Microscope (AFM).** The AFM images were recorded by Bruker Dimension

79 FastScan AFM with tapping mode tips (Dimension, resonant frequency: 1.4 MHz, force

80 constant: 18 N m^{-1}). We measured three 1×1 μm and three 5×5 μm images on three substrates

81 for each type of surfaces. The AFM software NanoScope Analysis (version 1.8) was used to

82 analyze the AFM images for topography and the rms roughness.

83 **X-ray Photoelectron Spectroscopy (XPS) Measurements.** XPS was used to characterize the

84 SAMs of HSC_m and $HS(Ph)_n$ with instruments located in National Center of Electron

85 Spectroscopy in Beijing. The energy of the incident X-ray beam (1486.6 eV) was used with the

86 Thermo Scientific K-Alpha XPS system. We recorded the high-resolution XPS spectra of S $2p$,

87 C $1s$ and Au $4f$. In analysis, we used the least-square peak fit with a pseudo-Voigt function (a

88 linear combination of Lorentzian (30%) and Gaussian (70%) functions)[4] to fit the XPS spectra

89 with Avantage software, and the sloping background was modelled using a smart background

90 correction.

91   The physical absorbed molecules with binding energy being about 161eV of S $2p$

92 spectrum[5] can be observed for $HS(Ph)_n$ (n = 1, 2, 3) anchored on Au^{DE} electrode with rms

93 roughness being 3.2nm (Fig. S24). In contrast, HSC_m, based on S $2p$ spectrum (Fig. S26), were

94 relatively densely assembled without physical absorbed molecules on rough Au substrate,

95 indicating that the topography of bottom-electrode had more remarkable impacts on packing of

96 conjugated molecules, the explanations of which was that $HS(Ph)_n$ SAMs anchored on rough

97 bottom-electrode with extremely deteriorated packing and destroyed $\pi - \pi$ interactions of

98 $HS(Ph)_n$ for their more rigid nature.

99 **Ultraviolet Photoelectron Spectroscopy (UPS) Measurements.** Work functions (WF) and

100 HOMO energy were detected by UPS function installed in the Thermo Scientific K-Alpha XPS

101 system. A specially designed biasing stage, which is in electrical contact with the analyzer, was

102 applied to hold the samples. All measurements were performed in an ultrahigh vacuum chamber

103 with a base pressure of 1×10^{-8} pa. To probe the valence band, the photon energy at 21.22 eV

104 was used and -10 V bias was applied to the sample to overcome the work function of the

105 analyzer. All UPS spectra were referenced to the Fermi edge of Au.

106

107 **S4. Electrical and thermoelectrical measurements**.

108 **Electrical Measurements and Analysis.** We followed previously reported procedures [2] to

109 form the SAM-based junctions with cone-shaped tips of Ga_2O_3/EGaIn. The Au substrate was

110 grounded and the top-electrode was biased from 0V → 0.5 V → 0V → -0.5 V → 0V, with a

111 step size of 50 mV, and a delay of 0.1 s, in all of our experiments. We measured three substrates

112 to obtain ≥20 junctions, for each of which we collected 20-24 $J(V)$ traces (that is a total of ~480

113 $J(V)$ traces for each type of SAM). The $J(V)$ data was analyzed following previously reported

114 procedures. [6] Briefly, we plotted the histogram of log|J| for each bias and fitted Gaussians to

115 the histograms to obtain the log-mean (μ_{log}) of the values of J and their log standard-deviations

116 (σ_{log}).

117 **Analysis of relationship between measured ΔV and S.** A polyimide (PI) film embedded with

118 heating resistors is used to heating the Au electrode to generate temperature difference

119 ($\Delta T = 0\sim8$ K) across the junctions (Fig. 1a, b). Firstly, control experiments were performed on

120 clean Au surfaces with different surface roughness that were absent of molecules (Fig. S7, S9).

121 We supposed that the temperature difference was mainly distributed across EGaIn and tungsten

122 tip (W tip) because the thermal conductivity of EGaIn ($G_{th, EGaIn}$ ~26.43 W m^{-1} K^{-1})[7] is far

123 overweight that of the surrounding air (~0.024 W m^{-1} K^{-1}). Wherein at Fig. S5, the difference

124 between V_1 and V_3 represents the measured ΔV, T_1 and T_3 denote room temperature. V_2 and T_2

125 are the potential and temperature measured by thermocouple of Au surface, respectively.

126 Therefore, the relationship between measured ΔV and S for Au/EGaIn junctions can be generally

127 depicted as Equation. (S1-S4)
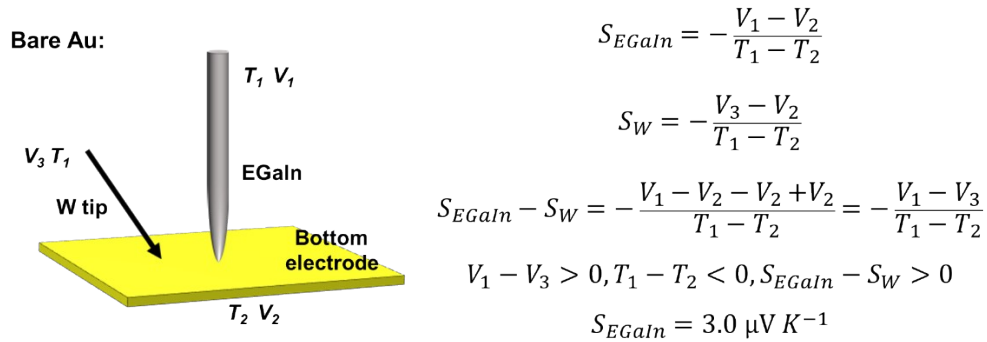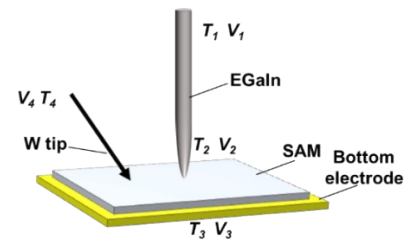
$$S_{EGaIn} = -\frac{V_1 - V_2}{T_1 - T_2} \tag{S1}$$

128

$$S_W = -\frac{V_3 - V_2}{T_1 - T_2} \tag{S2}$$

129

$$V_1 - V_3 > 0, \; T_1 - T_2 < 0, \; S_{EGaIn} - S_W > 0 \tag{S3}$$

130

$$S_{EGaIn} - S_W = -\frac{V_1 - V_2 - V_2 + V_2}{T_1 - T_2} = -\frac{V_1 - V_3}{T_1 - T_2} \tag{S4}$$

131

132   Fig. S21-S22 shows plot of ΔV as a function of ΔT for Au/EGaIn junctions with different

133 surface roughness. It can be found that the measured thermoelectric voltage is nearly

134 independent with the surface roughness of bottom electrode, according to $S = -\frac{\Delta V}{\Delta T}$, and the

135 obtained S is ~2.0 μV K^{-1}. Considering the thermopower of W tip (S_W) is 1.0 μV K^{-1},[8] and

136 hence，the thermopower of EGaIn (S_{EGaIn}) is 3.0 μV K^{-1}.

137

$$S_{EGaIn} = -\frac{V_1 - V_2}{T_1 - T_2}$$

$$S_W = -\frac{V_3 - V_2}{T_1 - T_2}$$

$$S_{EGaIn} - S_W = -\frac{V_1 - V_2 - V_2 + V_2}{T_1 - T_2} = -\frac{V_1 - V_3}{T_1 - T_2}$$

$$V_1 - V_3 > 0, T_1 - T_2 < 0, S_{EGaIn} - S_W > 0$$

$$S_{EGaIn} = 3.0 \; \mu V \, K^{-1}$$

138

139 **Fig. S5.** Schematic diagram of the voltages and temperatures across bare Au/EGaIn junction.

140

141 In the case of SAMs anchoring on Au electrode (Fig. S6), we defined T_1, V_1 and T_4, V_4 were the

142 temperature (room temperature) and potential of Syringe and W tip away from SAMs,

143 respectively. T_2 and V_2 were the temperature measured by thermocouple potential of Syringe

144 close to SAMs. V_3 and T_3 are the potential and temperature of Au surface. Theoretically, the

145 temperature gradient was supposed to locate across SAMs because the thermal conductivity of

146 n-alkanethiolates (~18 pW/K)[9] was 3 orders of magnitude smaller than that of EGaIn

147 $(\Delta T_1 = (T_1 - T_2) \gg \Delta T_2 = (T_2 - T_3))$, however, the measured T_2 was higher than room temperature

148 and approximately half as T_3 probably due to heat radiation $(\Delta T = \Delta T_1 \approx \Delta T_2 = \frac{1}{2}\Delta T_3 = (T_1 - T_3))$.

149 Hence, the relationship between measured ΔV and S for Au/SAM//Ga$_2$O$_3$/EGaIn junctions can

150 be generally depicted as Equation. (S5-S9)

$$S_{EGaIn} = -\frac{V_1 - V_2}{T_1 - T_2} = -\frac{\Delta V_1}{\Delta T_1} \tag{S5}$$

151

$$S_{SAM} = -\frac{V_2 - V_3}{T_2 - T_3} = -\frac{\Delta V_2}{\Delta T_2} \tag{S6}$$

152

$$S_W = -\frac{V_4 - V_3}{T_4 - T_3} = -\frac{\Delta V_3}{\Delta T_3} \tag{S7}$$

153

$$S_{EGaIn} + S_{SAM} - 2S_W = -\frac{V_1 - V_4}{\Delta T} \tag{S8}$$

154

$$S_{SAM} = -\frac{V_1 - V_4}{\Delta T} - S_{EGaIn} + 2S_W = -\frac{V_1 - V_4}{\Delta T} - 1 \tag{S9}$$

155

156

157 **Fig. S6.** Schematic diagram of the voltages and temperatures across Au/SAM//Ga$_2$O$_3$/EGaIn junction.

158

159 **Thermopower of commercial silicon wafer.** To verify that our platform can measure

160 thermopower precisely, we measured the Seebeck effects of commercial silicon wafer by EGaIn

161 top-contacts, including P-type and N-type and the results are shown in Fig. S7-S8. It is evidence

162 that the thermoelectric voltage is positively-changed for P-type Si supporting holes transport

163 once heating bottom electrode, and negatively-changed for N-type Si owing to charge transport

164 being dominated by electrons. The measured values of S for N-type and P-type Si are 309.3 ±

165 7.8 µV K^{-1} and -286.3 ± 26.3 µV K^{-1}, respectively, similar to the reported values.[10] The sign

166 of S were determined by the nature of charge carriers with either electrons or holes. Fig. S8f

167 shows schematic diagram of thermoelectric test of Si, where a copper wire was attached to the

168 bottom surface of silicon wafer, ensuring that the carriers mainly migrate along the longitudinal

169 direction during test.

170
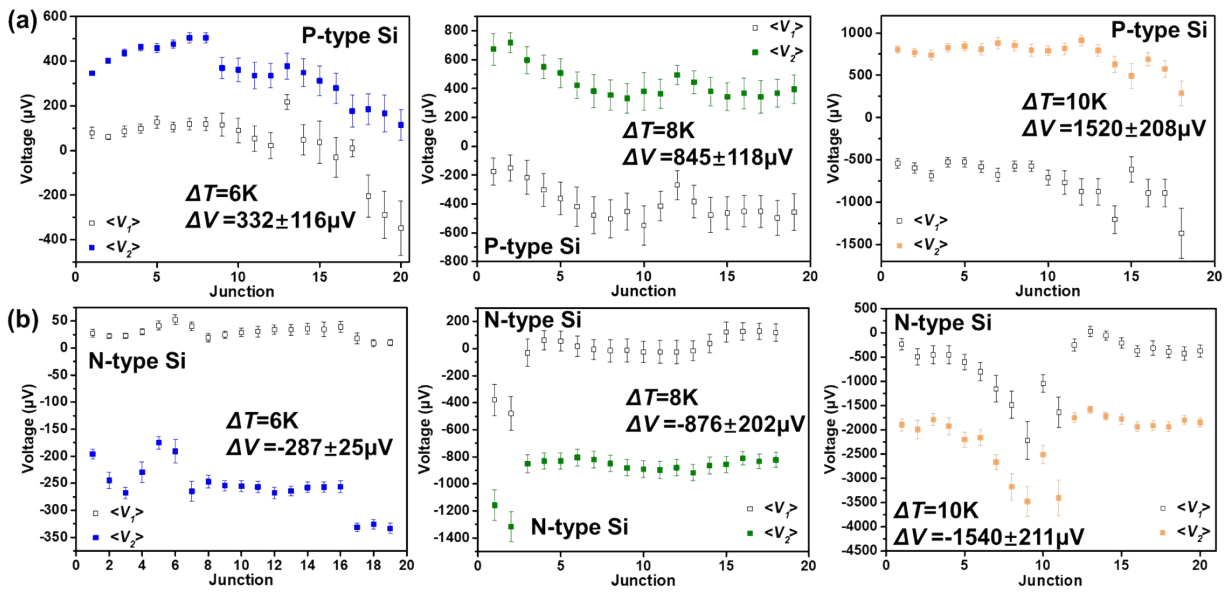
171

172 **Fig. S7.** Thermoelectric potential of Si//Ga$_2$O$_3$/EGaIn.

173
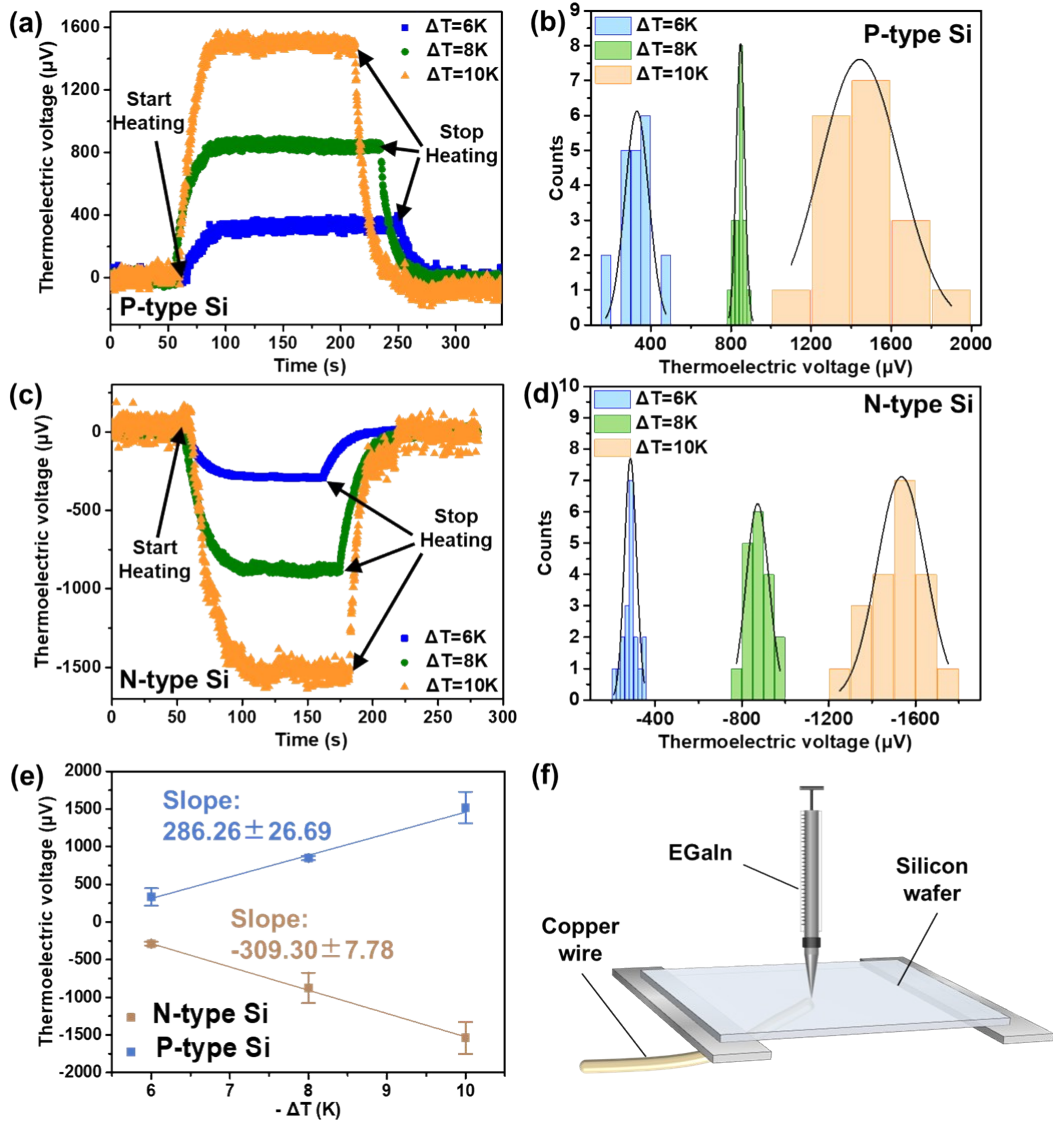
Fig. S8. Thermoelectric potential of Cu//Si//Ga$_2$O$_3$/EGaIn junction at different ΔT for P-type Si (a) and N-type Si (c), (b, d) corresponding histograms of ΔV with a Gaussian fit to these histograms, (e) plot of ΔV as a function of ΔT for of N-type and P-type Si, (f) Schematic diagram of thermoelectric test of Si, where a copper wire was attached to the bottom surface of the wafer.

The measurement accuracy and error analyses for Seebeck coefficient. The accuracy of our

thermal voltage measurement includes two parts: i) the accuracy of the output voltage and ii)

the accuracy of the input temperature. Firstly, Fig. S9 shows the accurate voltage measurement

was obtained by the voltmeter (2182A Nanovoltmeter, Keithley Inc., USA) with a detection

limit of 0.001μV. Considering the loss at the electrical circuit (mainly at the connection points),

so we take the significant digit of the thermovoltage in this work as 0.01μV.

S11

186

Fig. S9. The voltmeter (2182A NANOVOLTMETER, KEITHLEY Inc., America) we utilized to measure the voltage with accurate measurement of 0.001μV.

189

Secondly, the input temperature was monitored by a thermal couple with a detection limit of 0.01K. Therefore, we estimate the accurate significant digit of temperature was 0.1K in this study. Typical temperature-time trace is shown in Fig. S10. Wherein, T_1 is the room temperature, the average of T_1 ($<T_1>$) and its standard deviation could be obtained over ~100 s test duration with a Gaussian fit. Once we heated the bottom-electrode, ΔT occurred. When reaching thermal equilibrium, the average of T_2 ($<T_2>$) and its standard deviation could be obtained over ~200 s test time with a Gaussian fit. Then ΔT was obtained by using $<T_2>$ subtracting $<T_1>$. We recorded at least 20 junctions to generate a histogram of ΔT that can be fitted with Gaussians to determine the mean value of ΔT ($<\Delta T>$) and the corresponded standard-deviation, as shown in Fig. S10c. Hence, the error of ΔT is 0.1K, accounting for ~2.5%. Since the error of S originated from ΔV and ΔT, that of the former ($\sigma_{\Delta V}$) can be obtained from the results of linear fitting in Fig. 3 and the latter ($\sigma_{\Delta T}$) can be calculated from Fig. S10.

202
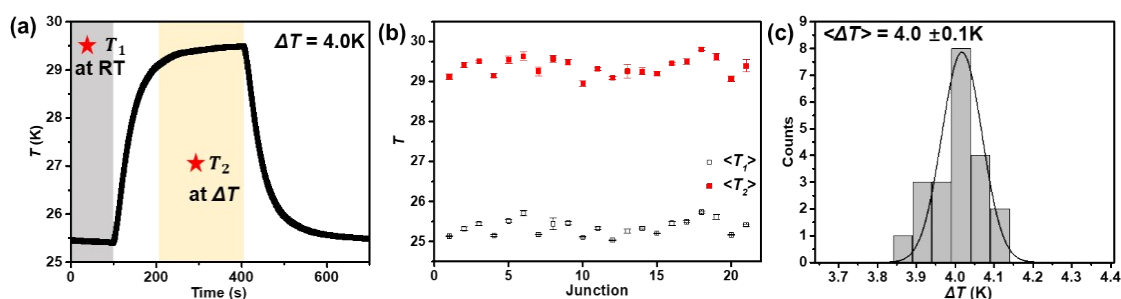
Fig. S10. (a) Temperature-time trace, (b) the related plot of ΔT against number of junctions, (c) the corresponded plot of histograms of $<\Delta T>$ (the mean value of ΔT) over 20 junctions with a Gaussian fit.

205 **Determination of power factor (PF).** We determined PF of HSC_m (m = 1, 2, 3) and $HS(Ph)_n$

206 (n = 1, 2, 3) according to a procedure reported in the literature.[11] The magnitude of electric field

207 intensity (E) can be given by:

$$E = \frac{V}{d} (GV\ m^{-1})$$

208 (S10)

209 where V is the applied voltage and d is the molecular length considering the tilt angle (30°) of

210 SAMs. The conductivity (σ) is the inverse of resistivity, and can be obtained as follows:

$$\sigma = \frac{J}{E} (\mu S\ cm^{-1})$$

211 (S11)

212 J (A cm^{-2}) is the current density. Using the calculated σ value and the measured S, the power

213 factor (PF) value was obtained according to the following relationship:

$$PF = S^2 \sigma\ (\mu W\ K^{-2}\ m^{-1}))$$

214 (S12)

215   It can be found that, based on UPS characterization (Table S1-S7), the location of HOMO

216 (E_{HOMO}) and energy offset (δE) were changed insignificantly for SAMs of HSC_m and $HS(Ph)_n$

217 with similar l, indicating the coincidence of corresponded electronic structure. Then, S and G

218 were lie on molecular length. $HS(Ph)_1$ with the smaller l (Table S8), possessed higher G than

219 that of HSC_4, and theoretically larger PF. However, the physical absorbed molecules with

220 binding energy being ~161eV of S $2p$ spectrum can be observed for $HS(Ph)_1$ anchored on Au

221 electrode (Fig. S24). In contrast, HSC_4, based on S $2p$ spectrum (Fig. S26), were relatively

222 densely assembled without physical absorbed molecules on Au^{TS} substrate. And the more rigid

223 nature of $HS(Ph)_1$ could deteriorate SAMs packing, leading to the reduced number of molecules

224 participating electron tunneling and lower S. In this case, the value of PF was dominated by S

225 for $HS(Ph)_1$ and HSC_4. In contrast, the l of $HS(Ph)_2$ and $HS(Ph)_3$ were larger than that of HSC_6

226 and HSC_8, respectively. In this case, PF of SAMs assembled on Au^{TS} electrode was mainly

227 depended on G. Increased molecular length contributed to the enhanced electron tunneling

228 distance and decreased G and inferior PF. Therefore, we qualitatively explain, from the

229 perspective of electron tunneling and molecular packing, that the PF of HSC_m was larger than

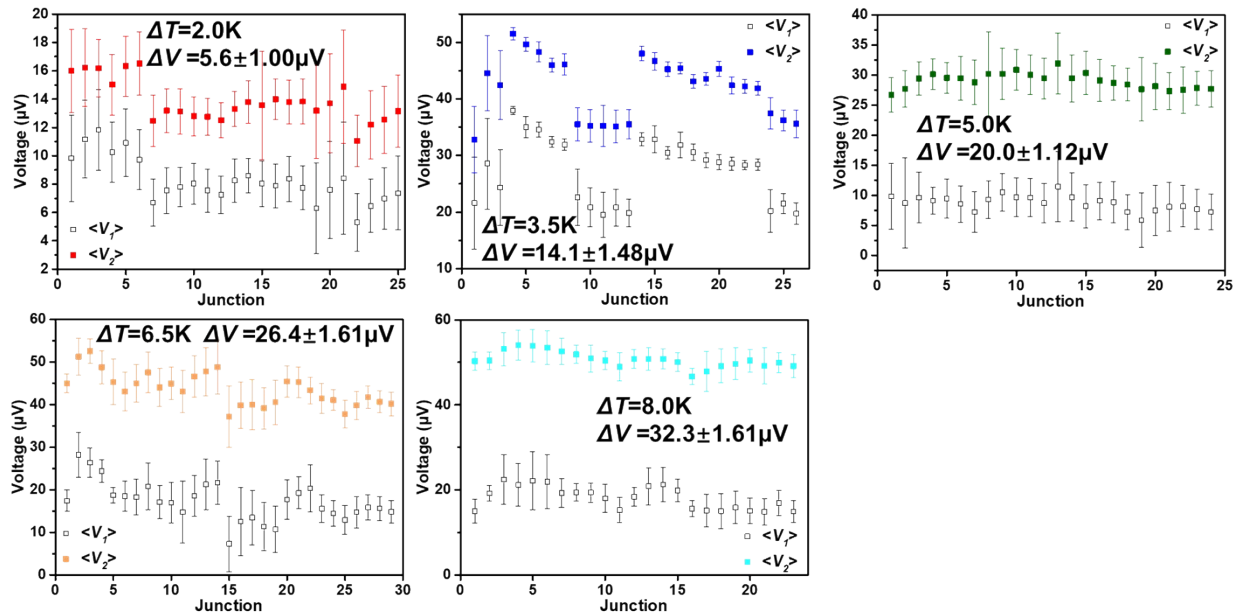230 that of similar molecular-length $HS(Ph)_n$ by combining XPS and UPS result.

231

232
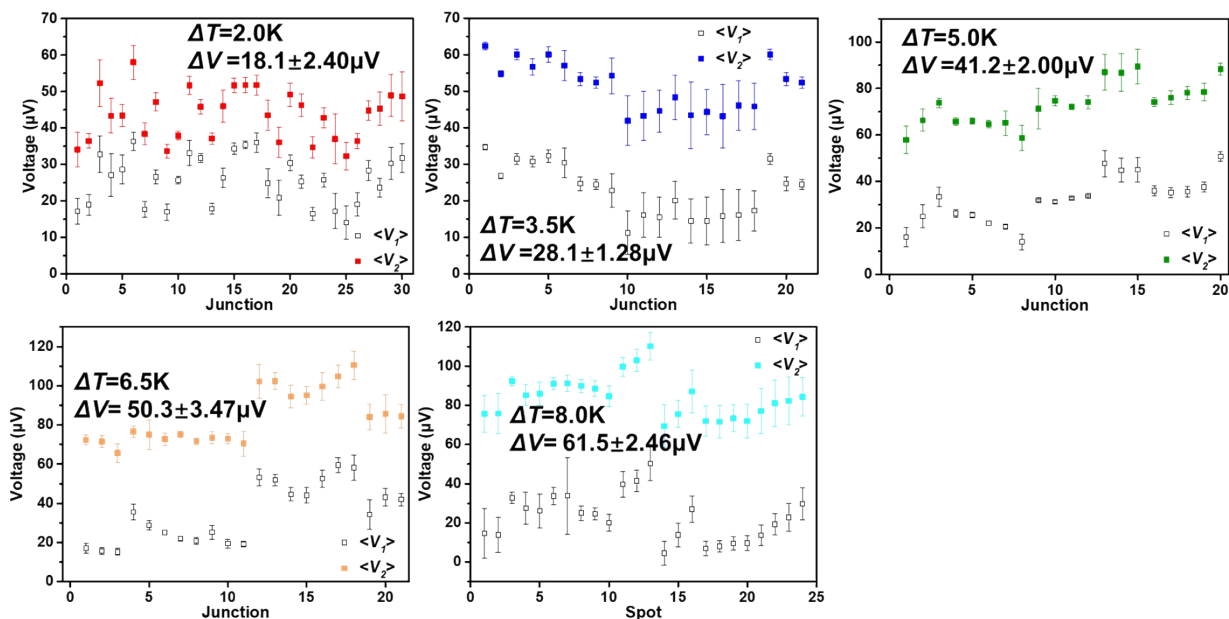
Fig. S11. The potential change of Au-$S(Ph)_2$//Ga$_2$O$_3$/EGaIn junctions for each spot with surface roughness
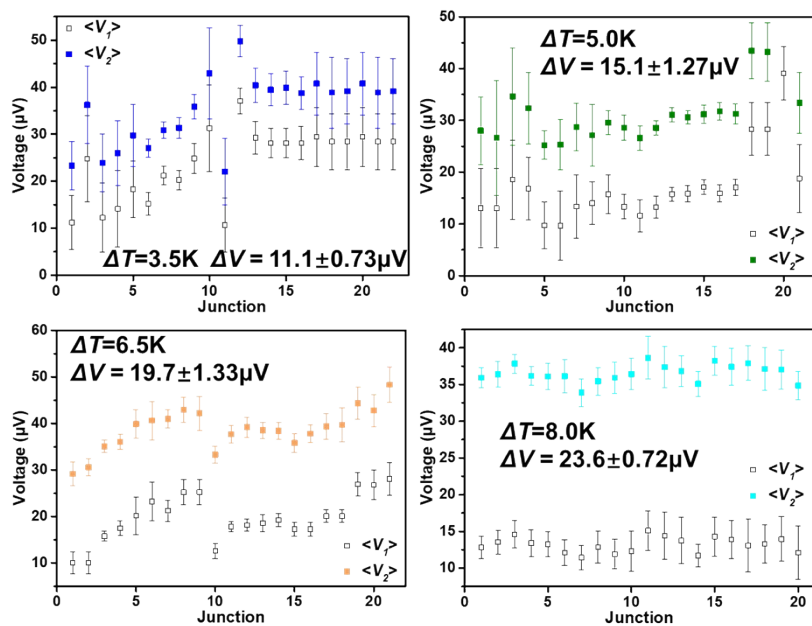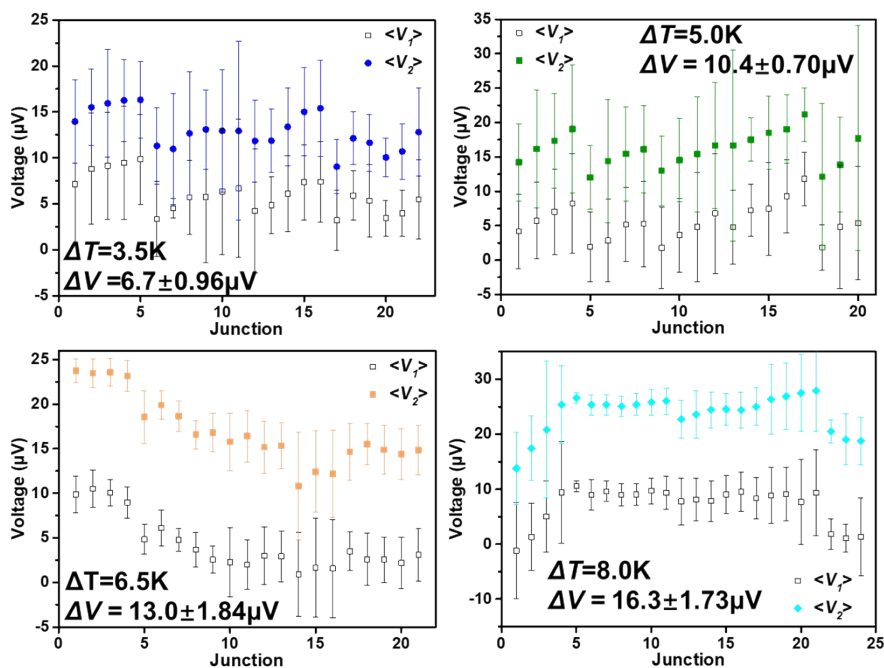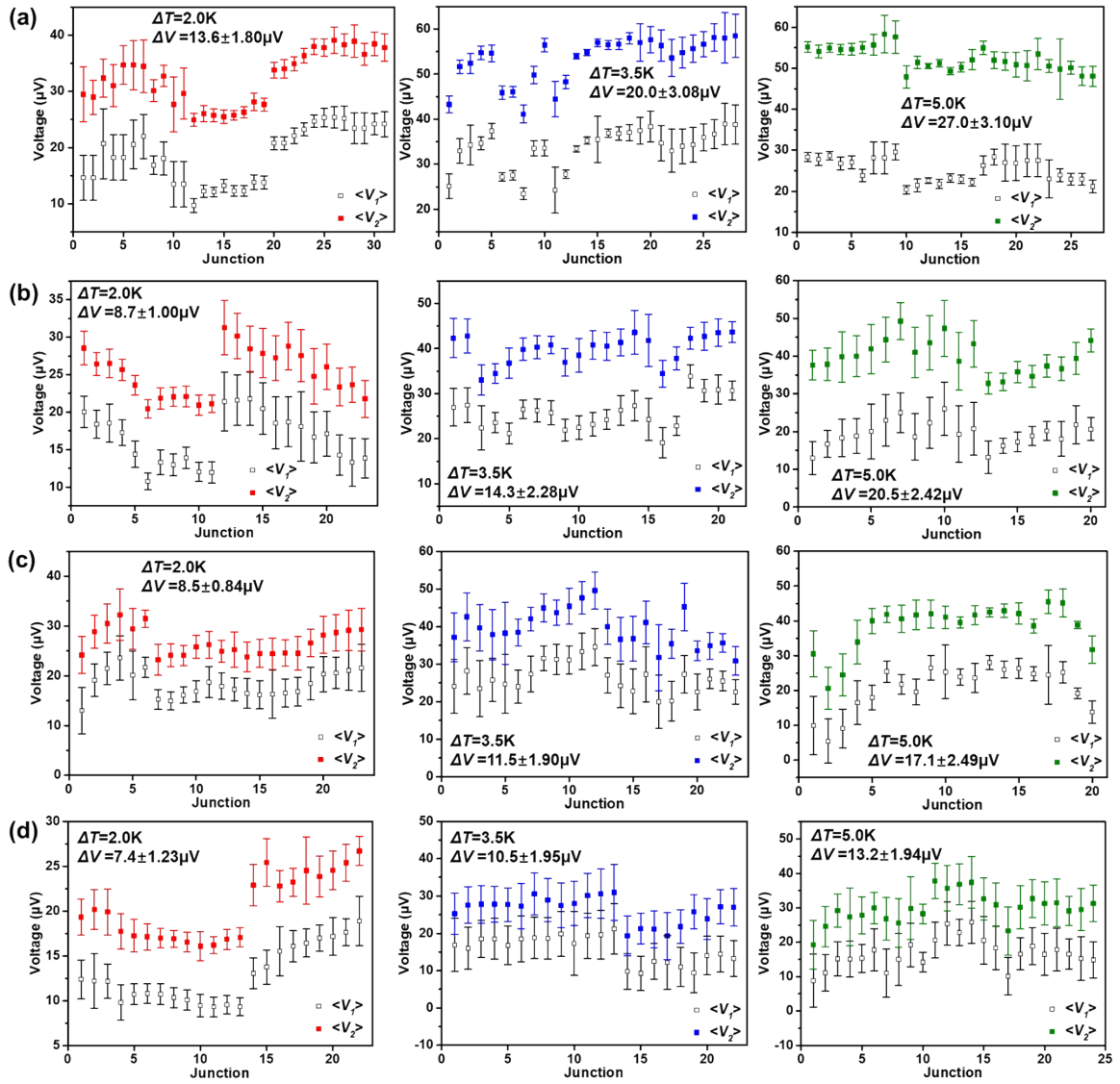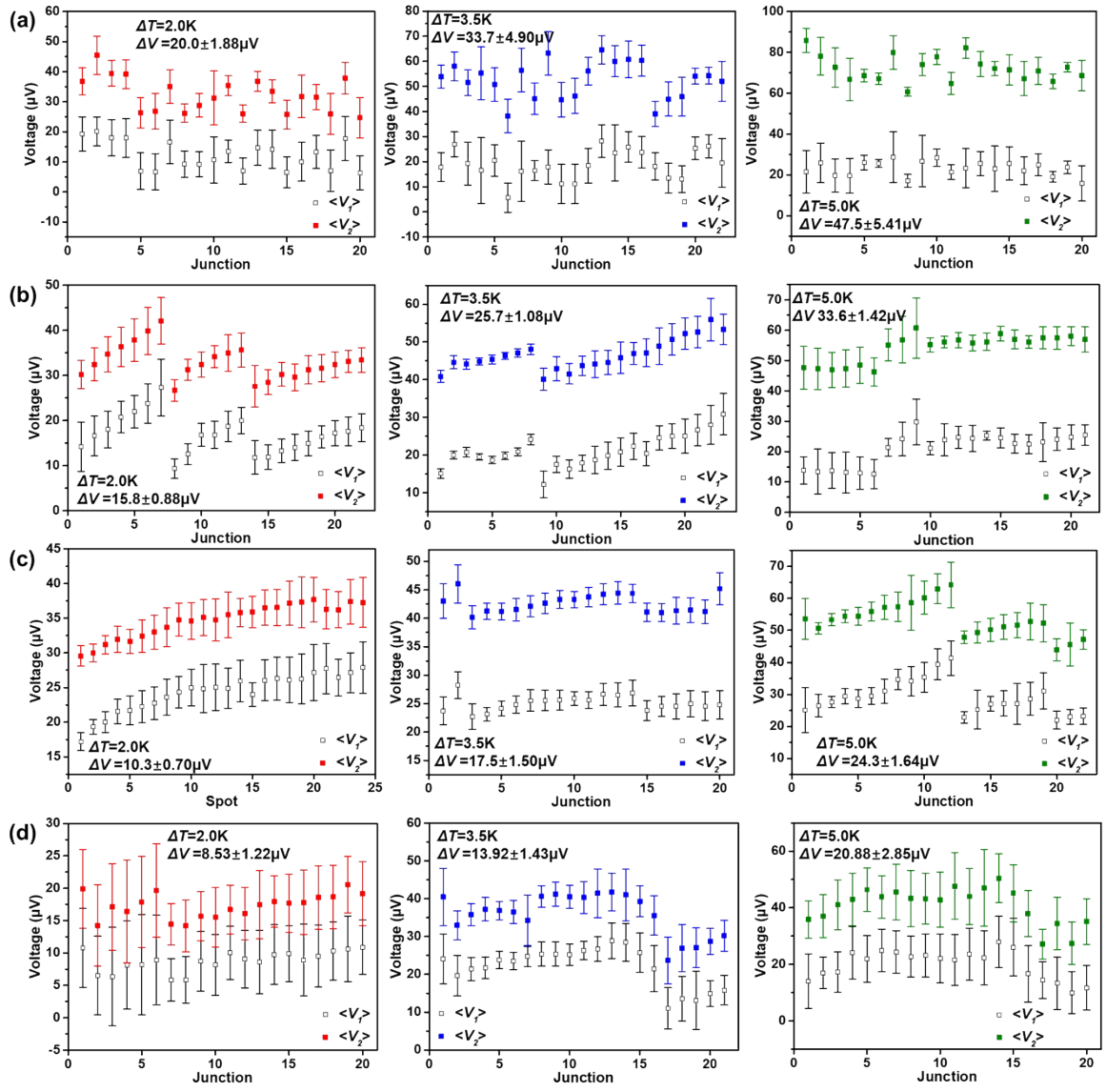of Au electrode being 0.37 nm.

235

236

Fig. S12. The potential change of Au-$S(Ph)_2$//Ga$_2$O$_3$/EGaIn junctions for each spot with surface roughness
of Au electrode being 1.30 nm.

239

240

Fig. S13. The potential change of Au-S(Ph)$_2$//Ga$_2$O$_3$/EGaIn junctions for each spot with surface roughness of Au electrode being 2.20 nm.

243

244

Fig. S14. The potential change of Au-S(Ph)$_2$//Ga$_2$O$_3$/EGaIn junctions for each spot with surface roughness of Au electrode being 3.20 nm.
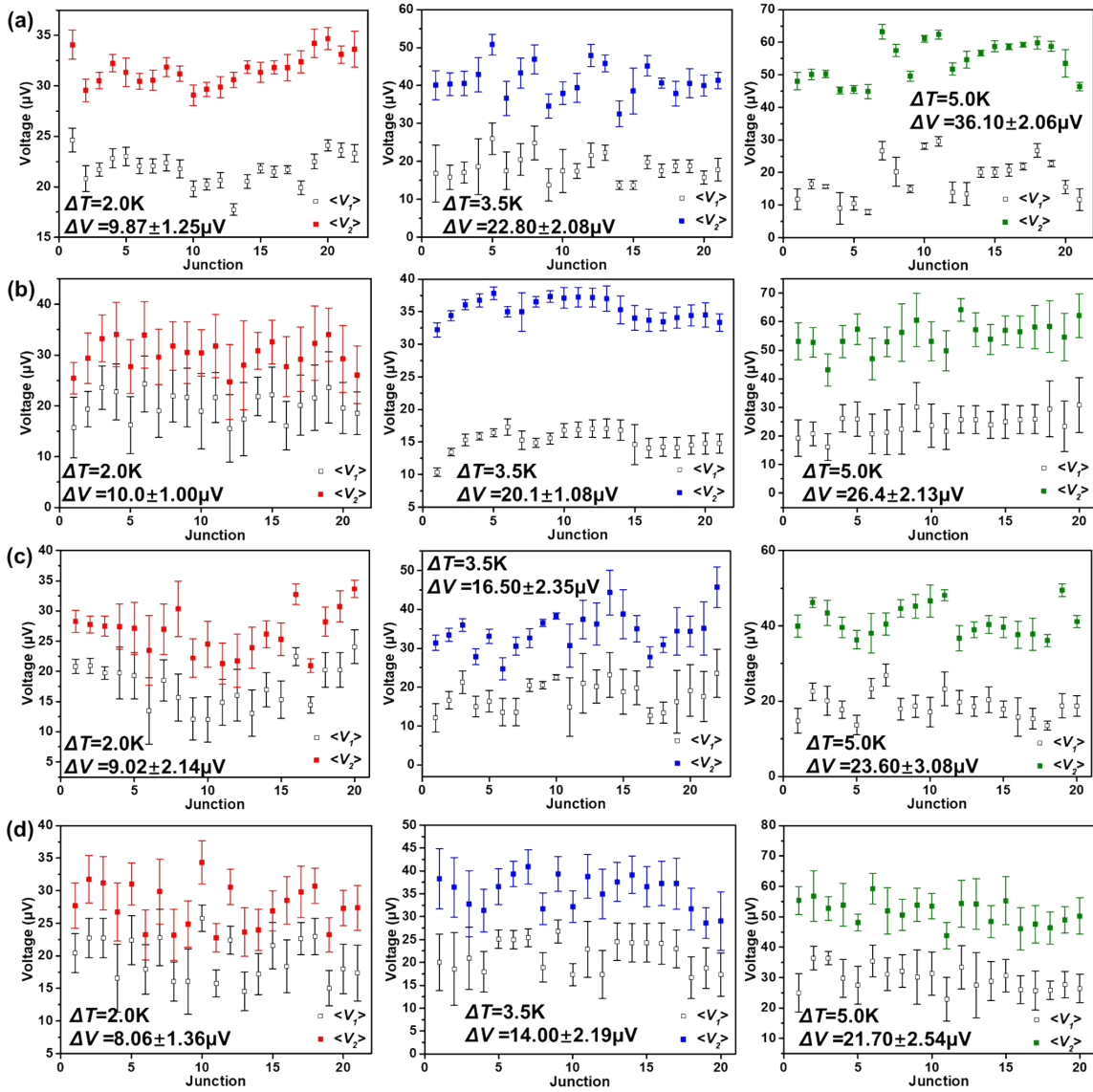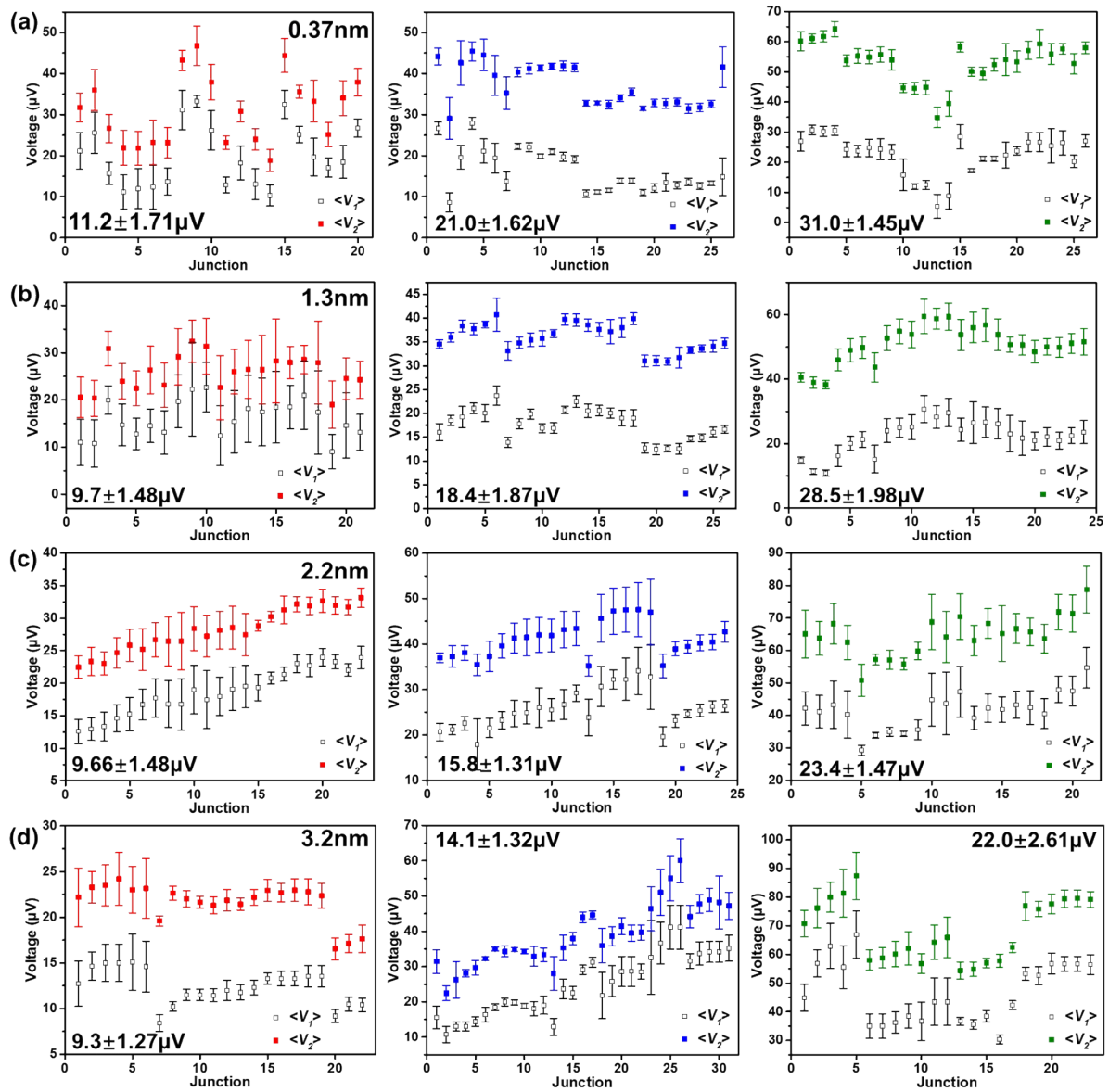
247

S15

Fig. S15. The potential change of Au-S(Ph)$_1$//Ga$_2$O$_3$/EGaIn junctions for each spot with surface roughness of Au electrode being (a) 0.37 nm, (b) 1.30 nm, (c) 2.20 nm and (d) 3.20 nm.

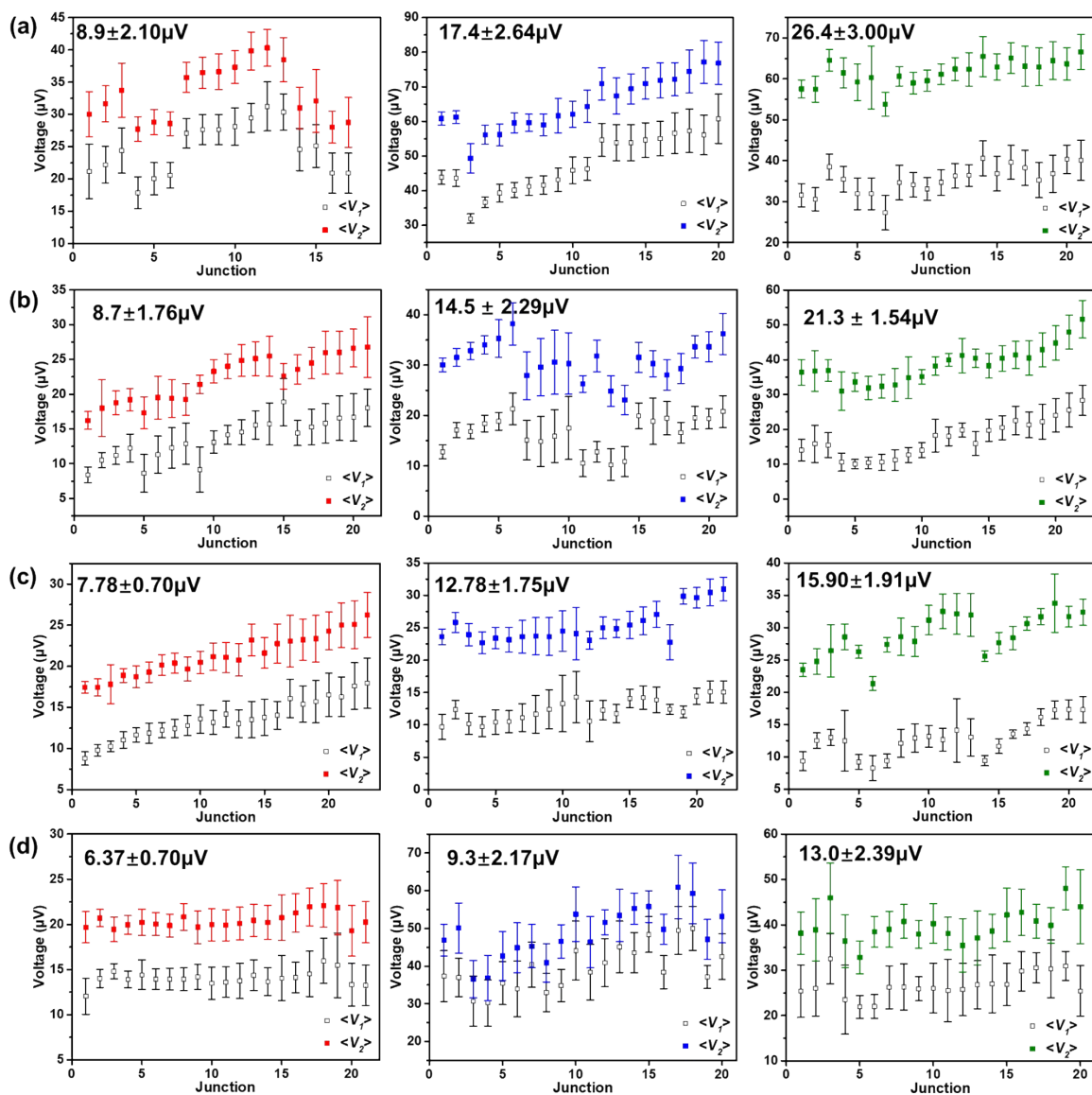**Fig. S16.** The potential change of Au-S(Ph)$_3$//Ga$_2$O$_3$/EGaIn junctions for each spot with surface roughness of Au electrode being (a) 0.37 nm, (b) 1.30 nm, (c) 2.20 nm and (d) 3.20 nm .

Fig. S17. The potential change of Au-SC$_4$//Ga$_2$O$_3$/EGaIn junctions for each spot with surface roughness of Au electrode being (a) 0.37 nm, (b) 1.30 nm, (c) 2.20 nm and (d) 3.20 nm .
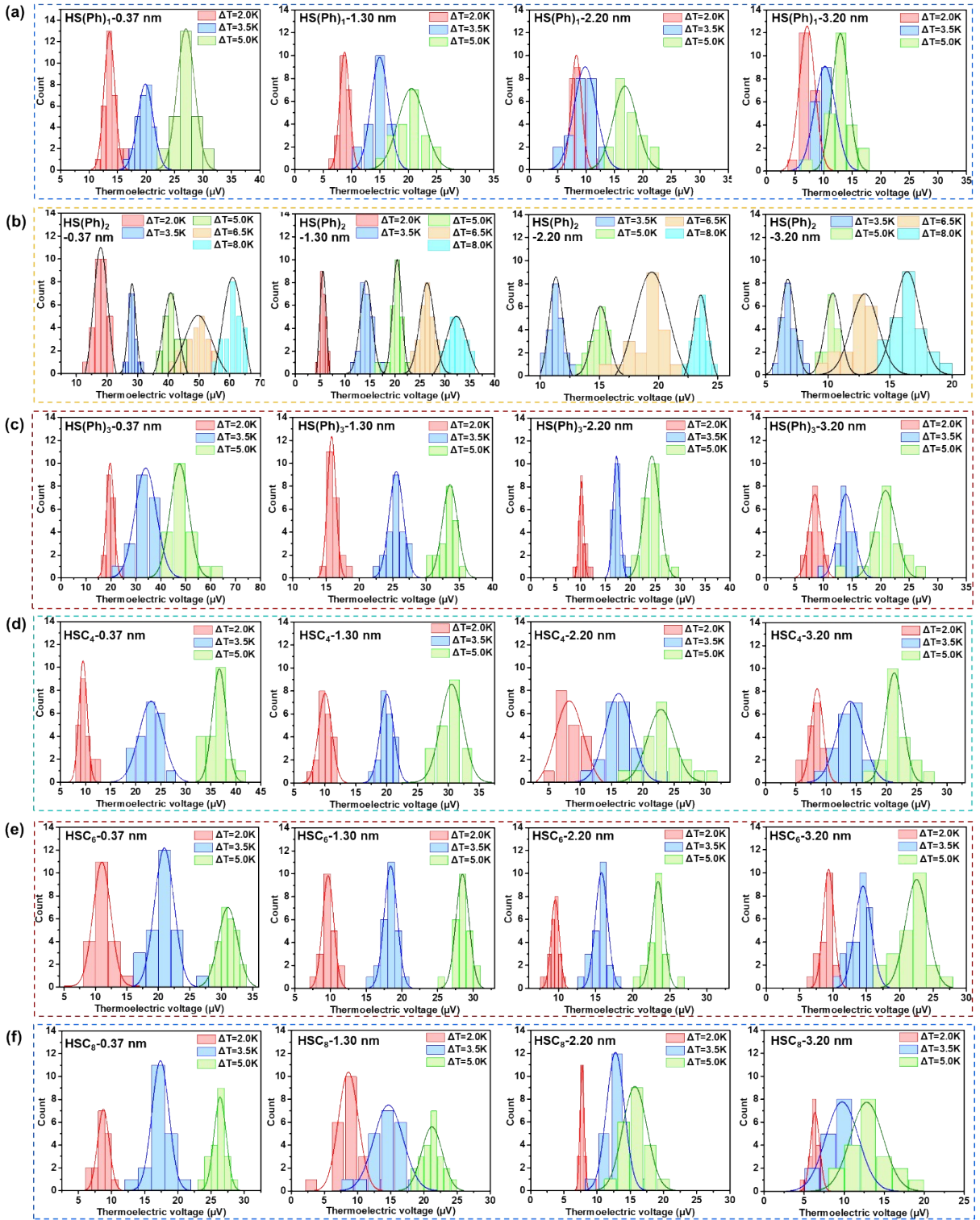
Fig. S18. The potential change of Au-SC$_6$//Ga$_2$O$_3$/EGaIn junctions for each spot with surface roughness of Au electrode being (a) 0.37 nm, (b) 1.30 nm, (c) 2.20 nm and (d) 3.20 nm.

Fig. S19. The potential change of Au-SC$_8$//Ga$_2$O$_3$/EGaIn junctions for each spot with surface roughness of Au electrode being (a) 0.37 nm, (b) 1.30 nm, (c) 2.20 nm and (d) 3.20 nm.

Fig. S20. The ΔV at each applied ΔT and the corresponding histograms of ΔV with a Gaussian fit to these histograms of Au-S(Ph)$_n$//Ga$_2$O$_3$/EGaIn and Au-C$_n$//Ga$_2$O$_3$/EGaIn with different surface roughness, including rms = 0.37 nm, rms = 1.30 nm, rms = 2.20 nm and rms = 3.20 nm.
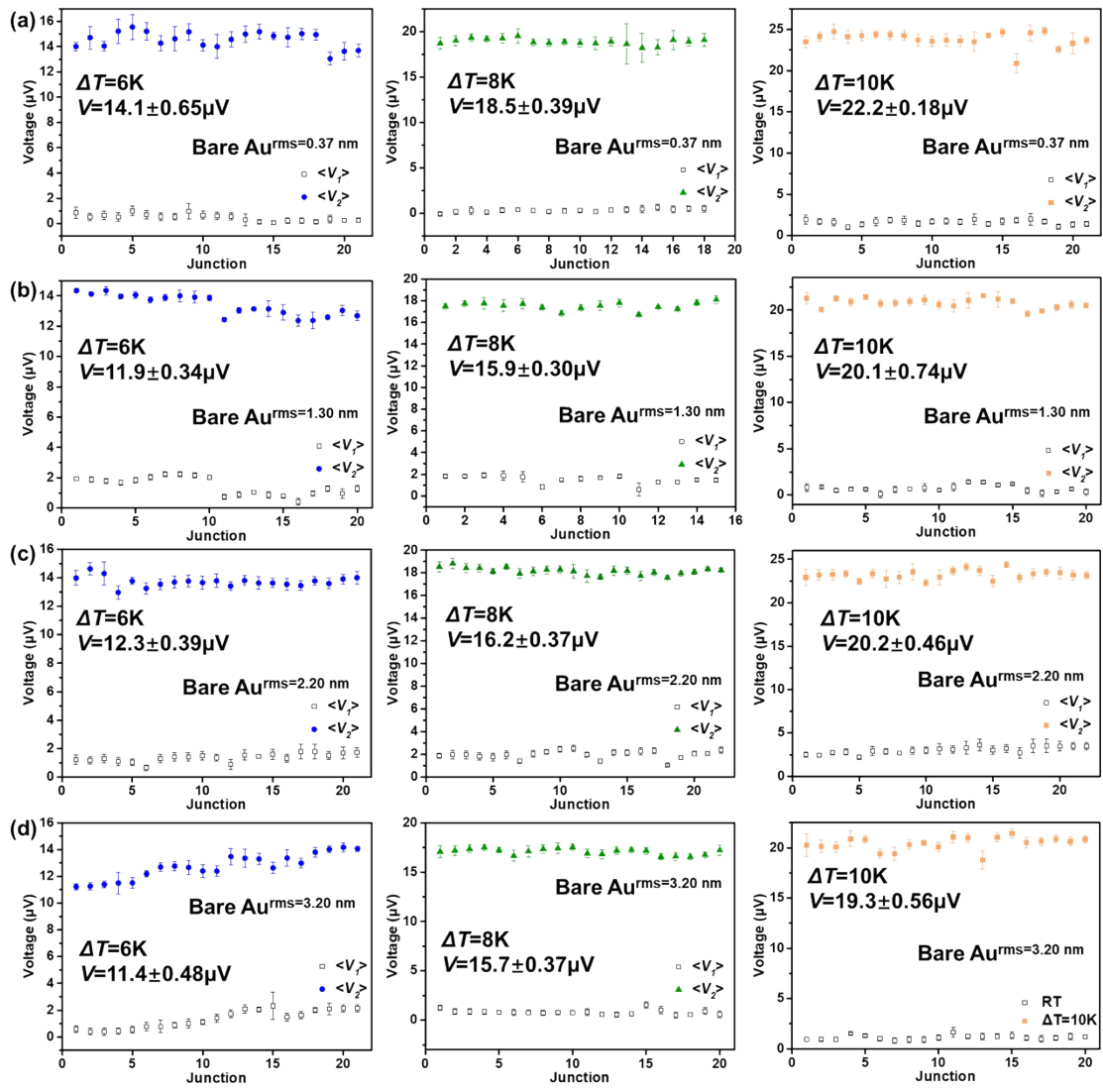
Fig. S21. The potential change of Au/EGaIn junction for each spot with different surface roughness, (a) rms = 0.37 nm, (b) rms = 1.30 nm, (c) rms = 2.20 nm and (d) rms =3.20 nm.
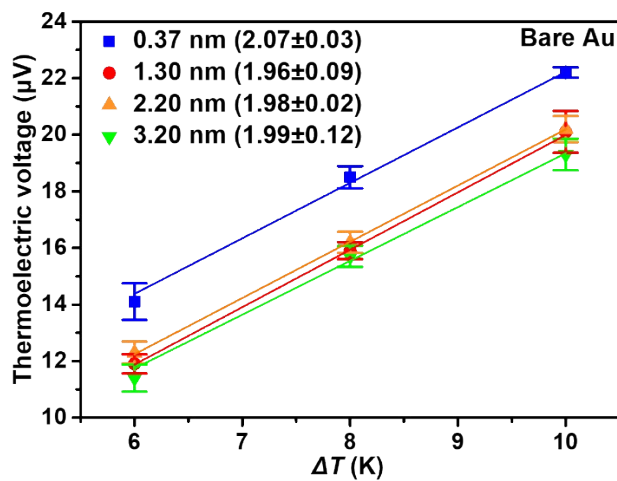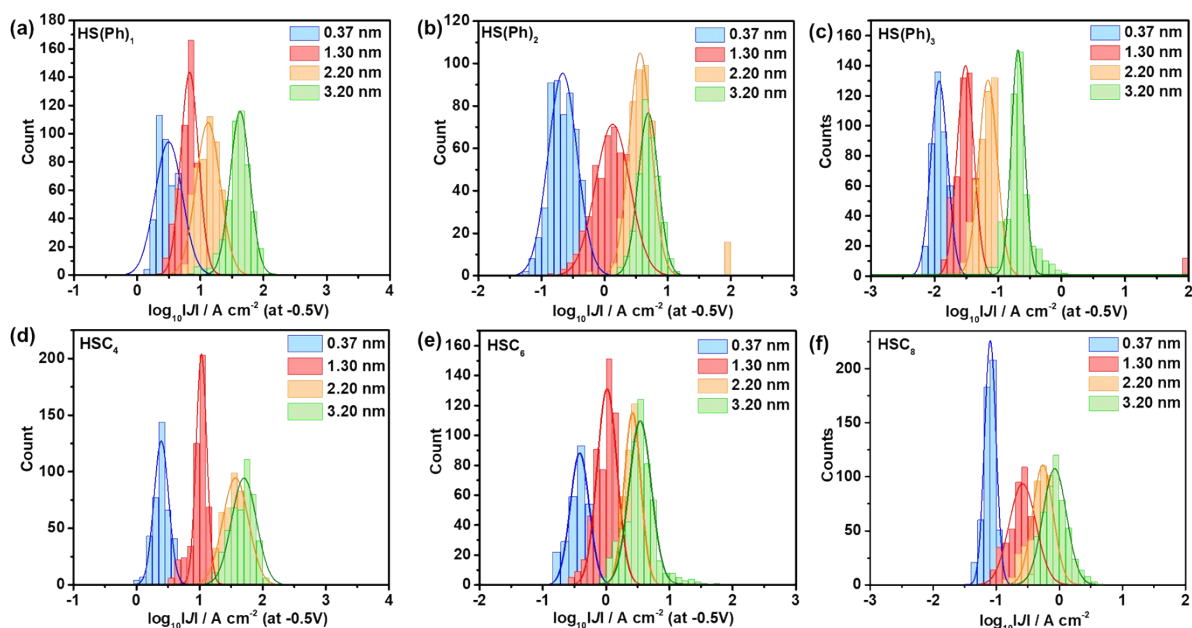

Fig. S22. Plot of ΔV as a function of ΔT of Au/EGaIn junctions with different surface roughness. The solid lines are the linear fit.
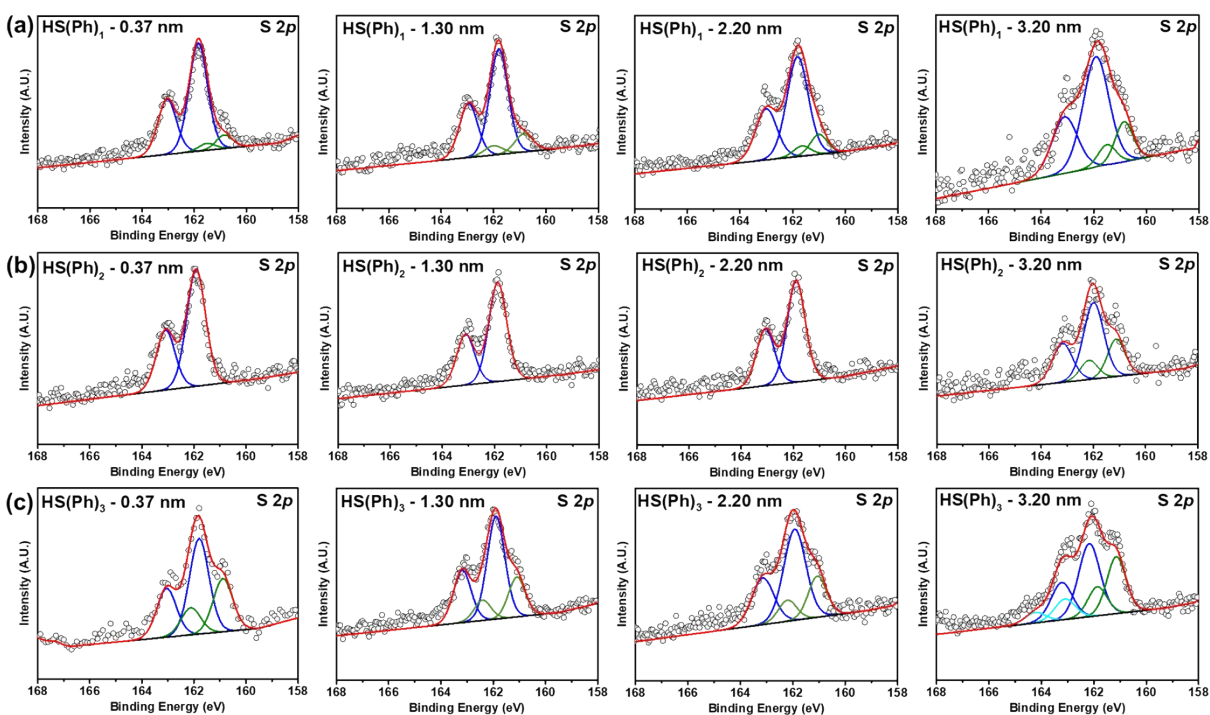
283

Fig. S23. The histograms of $\log_{10}|J|$ at -0.5V with Gaussian fits for Au- $S(Ph)_2//Ga_2O_3/EGaIn$, where rms = 0.37 nm, 1.30 nm, 2.20 nm, 3.20 nm.
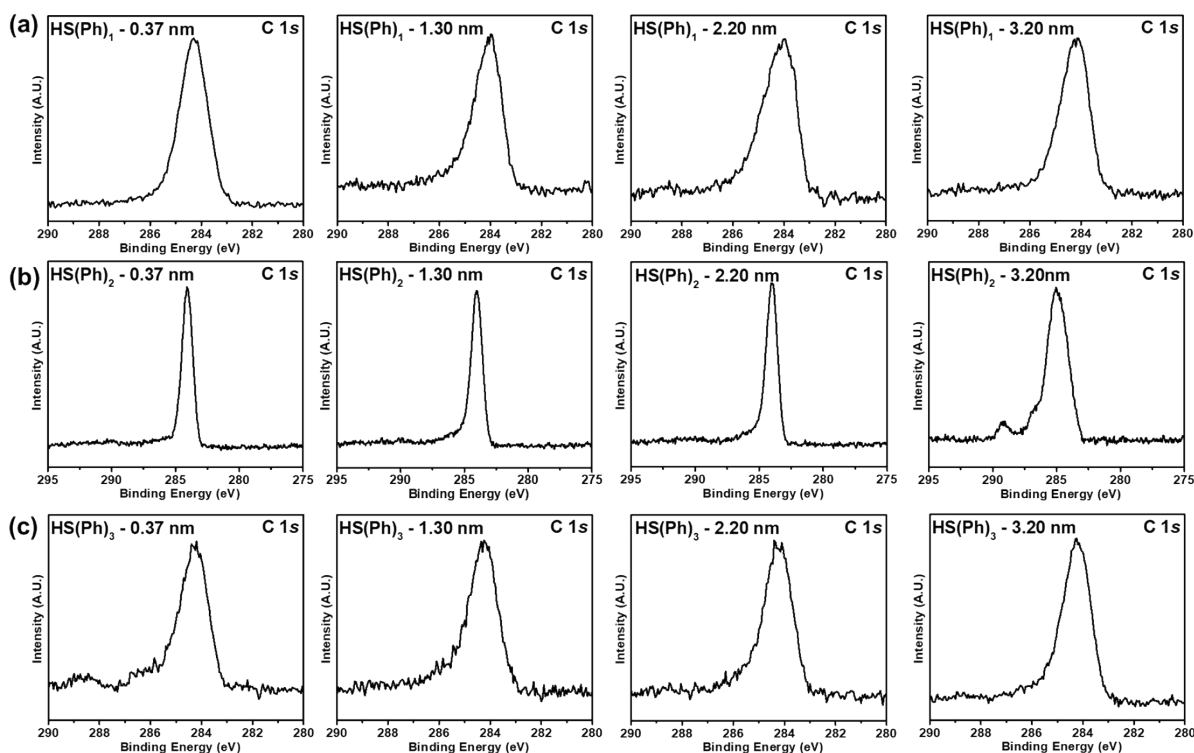
286

287

Fig. S24. The high resolution XPS S $2p$ spectra for Au-$S(Ph)_n$ (n = 1, 2, 3) with different surface roughness, including rms = 0.37 nm, 1.30 nm, 2.20 nm, 3.20 nm.

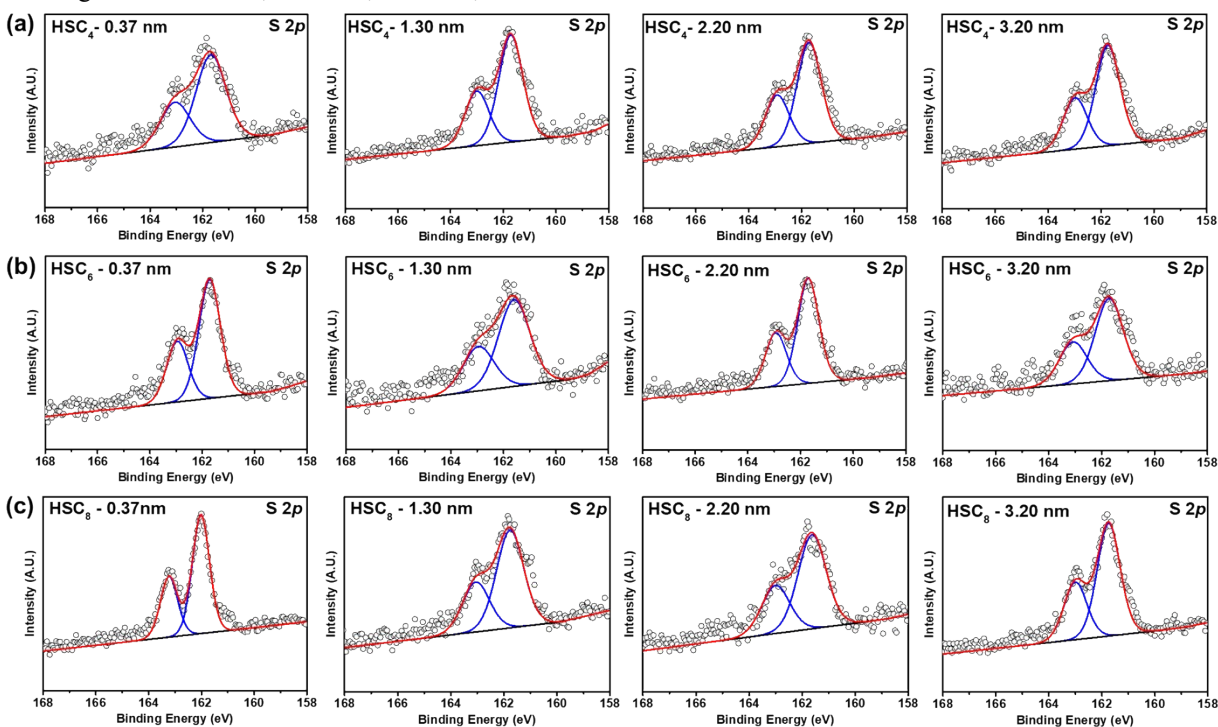290
291

292

Fig. S25. The high resolution XPS C 1*s* spectra for Au-S(Ph)$_n$ (n = 1, 2, 3) with different surface roughness, including rms = 0.37 nm, 1.30 nm, 2.20 nm, 3.20 nm.

295

Fig. S26. The high resolution XPS S 2*p* spectra for Au-SC$_m$ (m = 4, 6, 8) with different surface roughness, including rms = 0.37 nm, 1.30 nm, 2.20 nm, 3.20 nm.

303

304

Fig. S27. The high resolution XPS C 1*s* spectra for Au-SC$_m$ (m = 4, 6, 8) with different surface roughness, including rms = 0.37 nm, 1.30 nm, 2.20 nm, 3.20 nm.

307

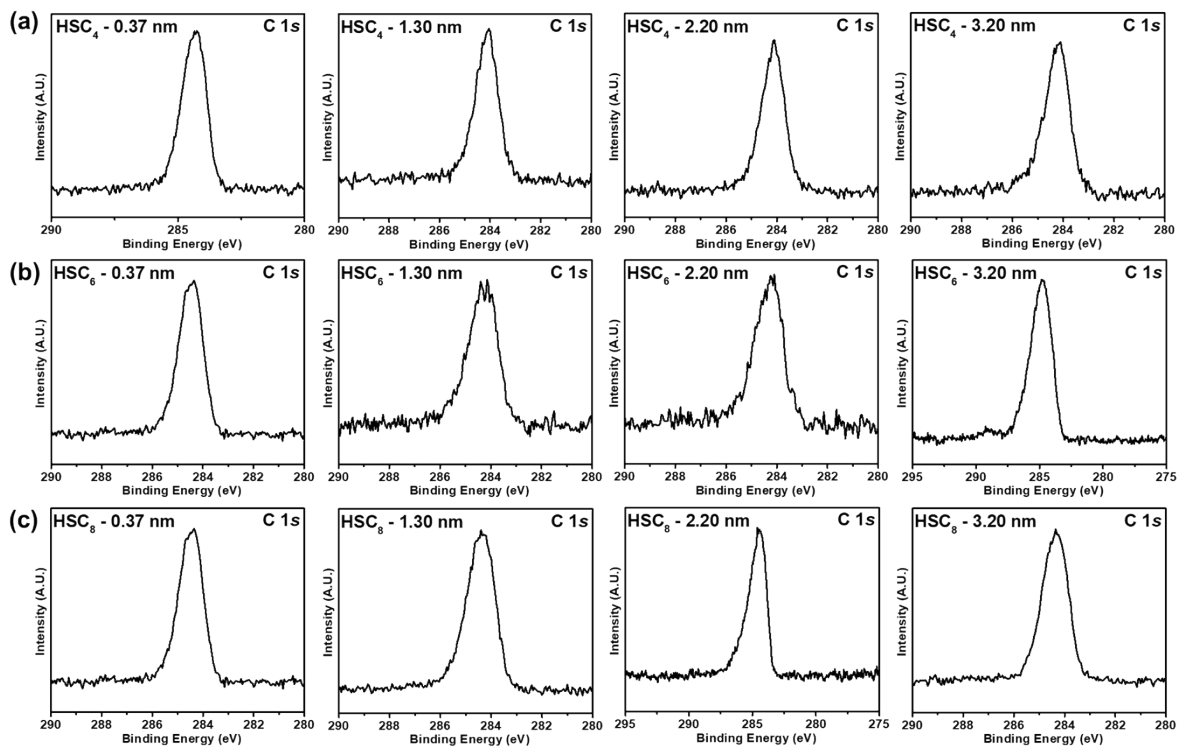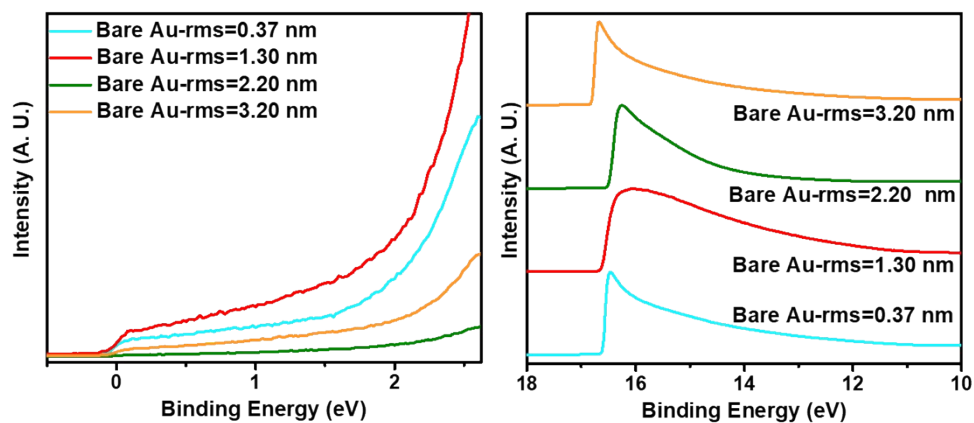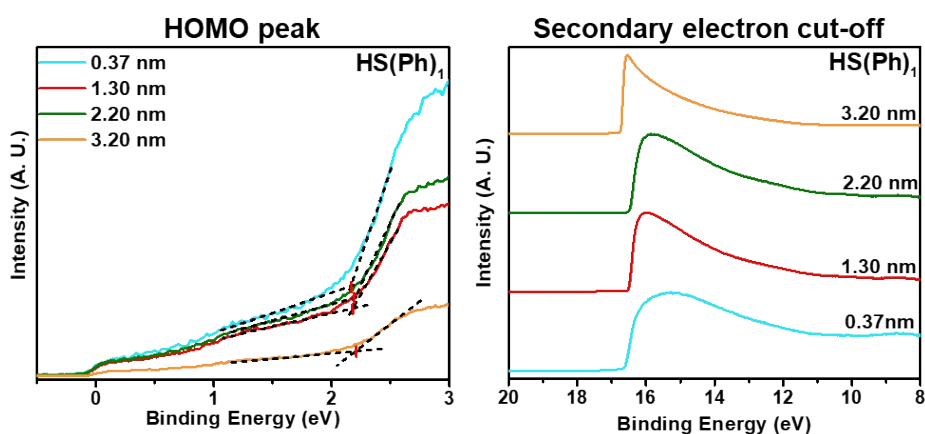308

Fig. S28. Ultraviolet photoemission spectroscopy (UPS) for bare Au with diverse rms.

310

311 **Table S1.** Properties of bare Au obtained by UPS.

Sample	$E_{\text{cut off}}$ (eV)	WF (eV)
rms=0.37 nm	16.61	4.61
rms=1.30 nm	16.63	4.59
rms=2.20 nm	16.50	4.72
rms=3.20 nm	16.70	4.52

312

313

314 **Fig. S29.** Valence band and secondary cutoff spectra of the HOMO peak for Au-S(Ph)$_1$ measured by UPS.

315

316 **Table S2.** Properties of Au-S(Ph)$_1$ SAMs obtained by UPS.

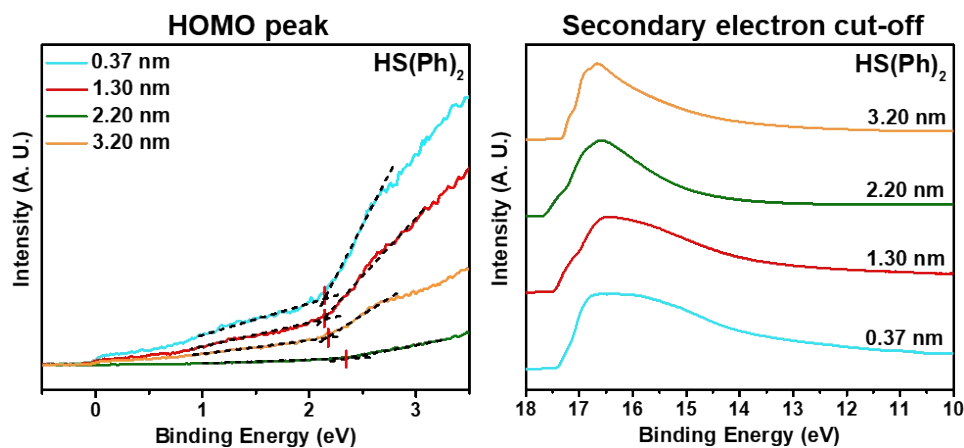| Sample	δE (eV)	$E_{\text{cut off}}$ (eV)	WF (eV)	E_{HOMO} (eV)
rms=0.37 nm	2.17	16.64	4.58	-6.75
rms=1.30 nm	2.18	16.50	4.72	-6.90
rms=2.20 nm	2.20	16.47	4.75	-6.95
rms=3.20 nm	2.20	16.73	4.49	-6.69

317

318

319 **Fig. S30.** Valence band and secondary cutoff spectra of the HOMO peak for Au-S(Ph)$_2$ measured by UPS.

320

321 **Table S3.** Properties of Au-S(Ph)$_2$ SAMs obtained by UPS.

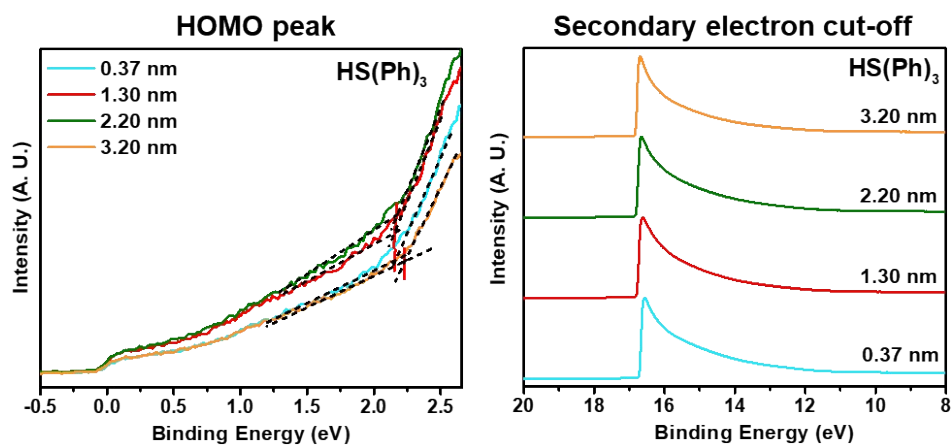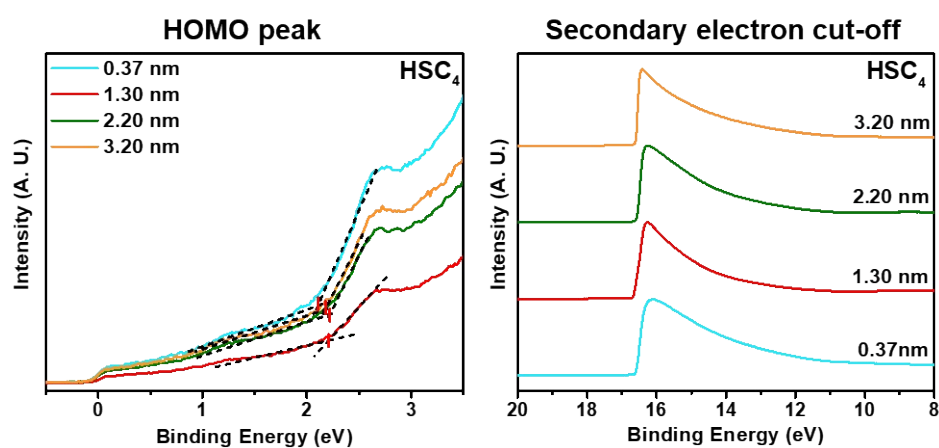| Sample	δE (eV)	$E_{\text{cut off}}$ (eV)	WF (eV)	E_{HOMO} (eV)
rms=0.37 nm	2.14	17.40	3.82	-5.96
rms=1.30 nm	2.13	17.48	3.74	-5.87
rms=2.20 nm	2.34	17.66	3.56	-5.90
rms=3.20 nm	2.16	17.31	3.91	-6.07

322

323

324 **Fig. S31.** Valence band and secondary cutoff spectra of the HOMO peak for Au-S(Ph)$_3$ measured by UPS.

325

326 **Table S4.** Properties of Au-S(Ph)₃ SAMs obtained by UPS.

Sample	δE (eV)	$E_{cut\ off}$ (eV)	WF (eV)	E_{HOMO} (eV)
rms=0.37 nm	2.15	16.72	4.50	-6.65
rms=1.30 nm	2.15	16.78	4.44	-6.59
rms=2.20 nm	2.19	16.82	4.40	-6.59
rms=3.20 nm	2.40	16.82	4.40	-6.80

327

328

329 **Fig. S32.** Valence band and secondary cutoff spectra of the HOMO peak for Au-SC₄ measured by UPS.

330 **Table S5.** Properties of Au-SC₄ SAMs obtained by UPS.

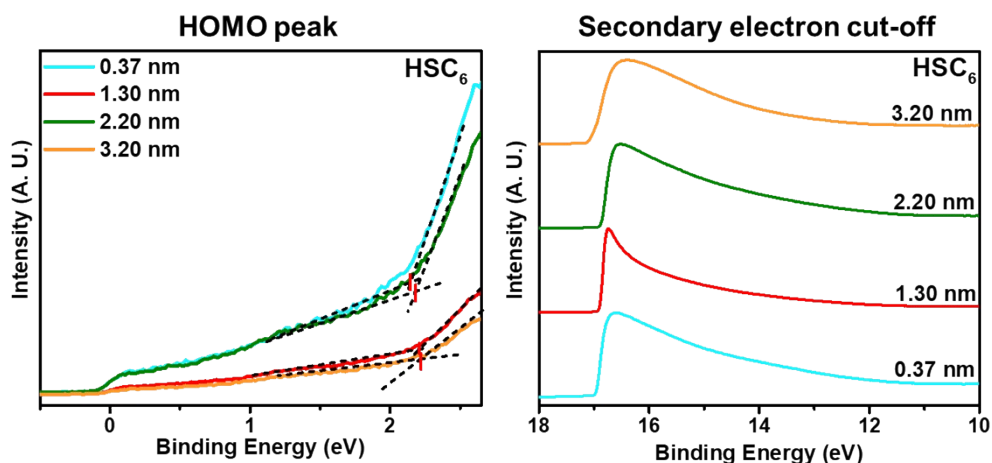| Sample	δE (eV)	$E_{cut\ off}$ (eV)	WF (eV)	E_{HOMO} (eV)
rms=0.37 nm	2.11	16.60	4.62	-6.73
rms=1.30 nm	2.21	16.63	4.59	-6.80
rms=2.20 nm	2.22	16.58	4.64	-6.86
rms=3.20 nm	2.17	16.61	4.61	-6.78

331

332

Fig. S33. Valence band and secondary cutoff spectra of the HOMO peak for Au-SC$_6$ measured by UPS.

Table S6. Properties of Au-SC$_6$ SAMs obtained by UPS.

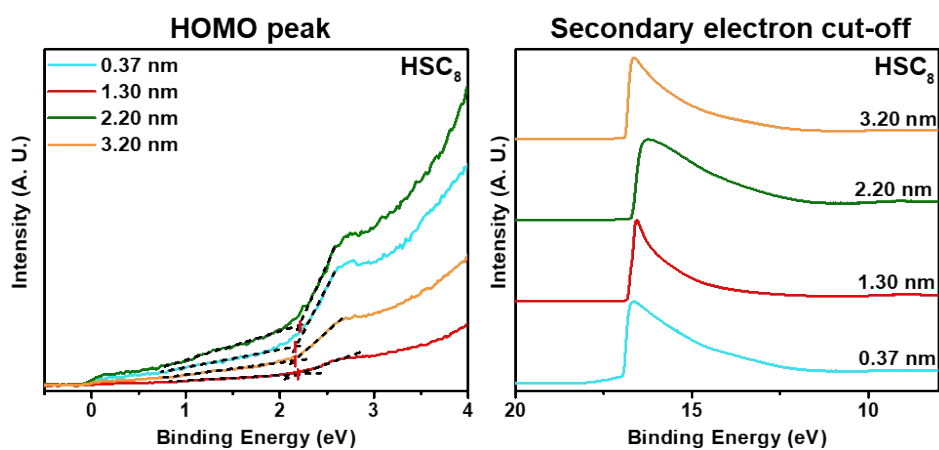| Sample	δE (eV)	$E_{cut\,off}$ (eV)	WF (eV)	E_{HOMO} (eV)
rms=0.37 nm	2.09	16.98	4.24	-6.33
rms=1.30 nm	2.17	16.91	4.31	-6.48
rms=2.20 nm	2.15	16.87	4.35	-6.50
rms=3.20 nm	2.24	17.06	4.16	-6.40

335

336

Fig. S34. Valence band and secondary cutoff spectra of the HOMO peak for Au-SC$_8$ measured by UPS.

338

339 **Table S7.** Properties of Au-SC$_8$ SAMs obtained by UPS.

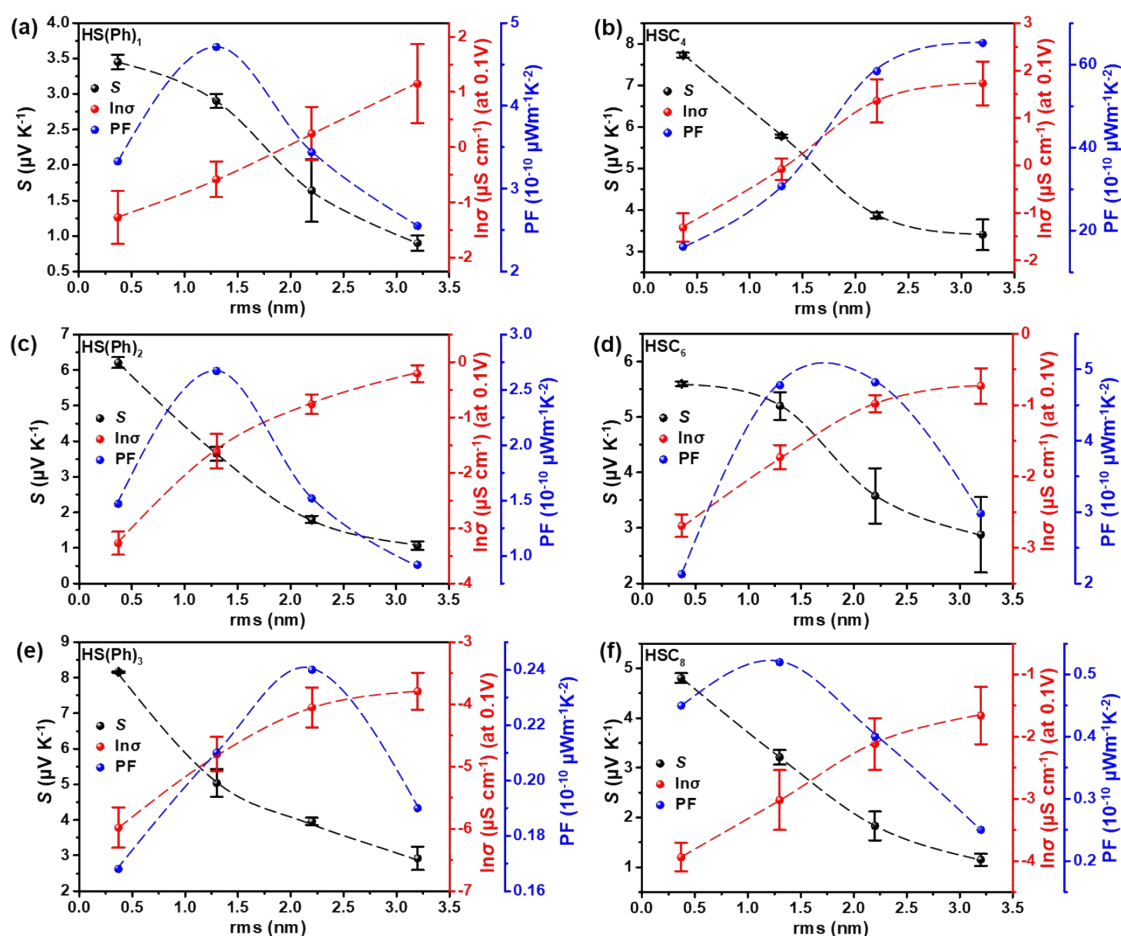| Sample	δE (eV)	$E_{cut\ off}$ (eV)	WF (eV)	E_{HOMO} (eV)
rms=0.37 nm	2.17	16.96	4.26	-6.43
rms=1.30 nm	2.19	16.84	4.38	-6.55
rms=2.20 nm	2.20	16.71	4.51	-6.71
rms=3.20 nm	2.15	16.88	4.34	-6.49

340
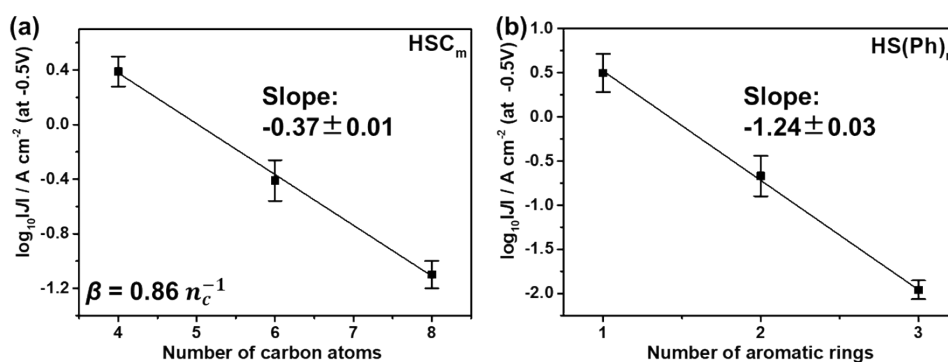
341

342 **Fig. S35.** Plots of log $|J|$ at -0.50 V versus number of carbon atoms or aromatic rings for junctions

343 incorporating SAMs of (a) HSC$_m$ (m = 4, 6, 8) and (b) HS(Ph)$_n$ (n = 1, 2, 3). The solid lines are fits to the

344 Simmons Equation.

345

Fig. S36. The power factor as a function of surface roughness. S, $\ln \sigma$ (at 0.1V) and PF as a function of rms roughness for HS(Ph)$_n$ (n = 1, 2, 3) and HSC$_m$ (m = 4, 6, 8). The dashed lines are a visual guide.

Table S8 Summary of molecular length (d) determined by ChemDraw software.

	HS(Ph)$_1$	HS(Ph)$_2$	HS(Ph)$_3$	HSC$_4$	HSC$_6$	HSC$_8$
l (Å)	4.59	8.72	12.92	5.27	7.82	10.37

References

1. Liu, Y.; Kim, J.; Seo, H.; Park, S.; Chae, J., Copper(II)-catalyzed single-step synthesis of Aryl thiols from Aryl halides and 1,2-ethanedithiol. *Adv.Synth. Catal.* **2015,** *357*, 2205.
2. Yuan, L.; Jiang, L.; Zhang, B.; Nijhuis, C. A., Dependency of the tunneling decay coefficient in molecular tunneling junctions on the topography of the bottom electrodes. *Angew. Chem. Int. Edit.* **2014,** *53*, 3377.

360 3.   Yuan, L.; Jiang, L.; Thompson, D.; Nijhuis, C. A., On the remarkable role of surface
361 topography of the bottom electrodes in blocking leakage currents in molecular diodes. *J. Am.*
362 *Chem. Soc.* **2014,** *136*, 6554.
363 4.   Doniach, S.; Sunjic, M., Many-electron singularity in X-ray photoemission and X-ray line
364 spectra from metals. *J. Phys. C Solid State Phys.* **1970,** *3*, 285.
365 5.   Kumar, S.; Soni, S.; Danowski, W.; van Beek, C. L. F.; Feringa, B. L.; Rudolf, P.; Chiechi,
366 R. C., Correlating the influence of disulfides in monolayers across photoelectron spectroscopy
367 wettability and tunneling charge-transport. *J Am. Chem. Soc.* **2020,** *142*, 15075.
368 6.   Nerngchamnong, N.; Yuan, L.; Qi, D. C.; Li, J.; Thompson, D.; Nijhuis, C. A., The role of
369 van der Waals forces in the performance of molecular diodes. *Nat. Nanotechnol.* **2013,** *8*, 113.
370 7.   Yu, S.; Kaviany, M., Electrical, thermal, and species transport properties of liquid eutectic
371 Ga-In and Ga-In-Sn from first principles. *J. Chem. Phys.* **2014,** *140*, 064303.
372 8.   Fiflis, P.; Kirsch, L.; Andruczyk, D.; Curreli, D.; Ruzic, D. N., Seebeck coefficient
373 measurements on Li, Sn, Ta, Mo, and W. *J. Nucl. Mater.* **2013,** *438*, 224.
374 9.   Cui, L.; Hur, S.; Akbar, Z. A.; Klockner, J. C.; Jeong, W.; Pauly, F.; Jang, S. Y.; Reddy, P.;
375 Meyhofer, E., Thermal conductance of single-molecule junctions. *Nature* **2019,** *572*, 628.
376 10. Rincón-García, L.; Evangeli, C.; Rubio-Bollinger, G.; Agraït, N., Thermopower
377 measurements in molecular junctions. *Chem. Soc. Rev.* **2016,** *45*, 4285.
378 11. Park, S.; Kang, S.; Yoon, H. J., Power factor of one molecule thick films and length
379 dependence. *ACS Cent. Sci.* **2019,** *5*, 1975.
380